mTOR inhibitor-independent Autophagy Activator Ameliorates Tauopathy and Prionopathy Neurodegeneration Phenotypes

Leonard Yoon[¥,1], Rachel C. Botham[¥,1], Adriaan Verhelle[¥,2], Pablo Sanz-Martinez[4], Jin Xu[1], Christian M. Cole[1], Ee Phie Tan[1], Ching Chieh Chou[12], Caroline A. Cuoco[1], Lynée A. Massey[1], Sergio Labra[1], Lisa P. Elia[6,7], Amina Ta[8], Maziar S. Ardejani[1], Kyunga Lee[1], Gabriel M. Kline[1], Qiang Xiao[1], Sara Cano-Franco[4], Nora J. Lyang[5], William C. Hou[1], Anan Yu[11], Susan Fox[11], Yeonjin Ko (Bollong lab), Cristian Wulkop-Gil[2], Lara H. Ibrahim[1], Starr Jiang[9], Alina Meneses[1], Luke T. Nelson[1], Hongfan Peng[1], Stuart A. Lipton[2], Michael J. Bollong[1], Malene Hansen[5], Richard I. Morimoto[11], H. Michael Petrassi[8], R. Luke Wiseman[12], Evan T. Powers[1], Steven Finkbeiner[6,7], Danny Garza[1], Daniel Finley[10], Miguel A. Prado[10], Ivan Dikic[4], Judith Frydman[12], Kristen A. Johnson*[,8], M. Catarina Silva*[,3], Stephen J. Haggarty*[,3], Alexandra Stolz*[,4], Sandra E. Encalada*[,2] and Jeffery W. Kelly*[,1]

[1]Department of Chemistry, Neurodegeneration New Medicines Center, and the Skaggs Institute of Chemical Biology, The Scripps Research Institute, La Jolla CA 92037 USA; [2]Departments of Molecular Medicine and Neurobiology, Neurodegeneration New Medicines Center, The Scripps Research Institute, La Jolla CA 92037 USA; [3]Chemical Neurobiology Laboratory, Center for Genomic Medicine, Department of Neurology, Massachusetts General Hospital and Harvard Medical School, 185 Cambridge Street CPZN 5400, Boston, MA 02114 USA; [4] Institute of Biochemistry 2 and Buchmann Institute for Molecular Life Sciences, Goethe University Frankfurt, 60590 Frankfurt am Main, Germany; [5]Sanford Burnham Prebys Medical Discovery Institute, La Jolla CA 92037 USA; [6]Gladstone Institute of Neurologic Disease, San Francisco, CA, USA; [7]Department of Neurology, University of California-San Francisco Medical Center, San Francisco, CA, USA; [8]Calibr, a Division of Scripps Research, 11119 North Torrey Pines Rd, La Jolla, CA 92037 USA; [9]Department of Biology, Stanford University, Stanford, CA, USA; [10]Department of Cell Biology, Harvard Medical School, Boston, MA 02115 USA;[11]Department of Biochemistry, Molecular Biology, and Cell Biology, Northwestern University Institute for Neuroscience, Rice Institute for Biomedical Research, Northwestern University, Evanston, Illinois 60208, USA; [12]Department of Molecular Medicine, The Scripps Research Institute, La Jolla, CA 92037 USA

Co-corresponding authors
Steven Finkbeiner: steve.finkbeiner@gladstone.ucsf.edu
Kristen A. Johnson: kajohnson@scripps.edu
M. Catarina Silva: mlimadasilva@mgh.harvard.edu
Stephen J. Haggarty: shaggarty@mgh.harvard.edu
Alexandra Stolz: stolz@em.uni-frankfurt.de
Sandra E. Encalada: encalada@scripps.edu
Jeffery W. Kelly: jwk@scripps.edu

Summary

Autophagy activation has the potential to ameliorate neurodegenerative disease phenotypes, including protein aggregation, lipid level perturbations and axonal trafficking defects. We performed a high content imaging-based screen assessing 940,000 small molecules to identify those that accelerate lipid droplet clearance. Hits were validated in diverse cell lines and by counter-screening. Of the 77 validated structurally diverse hits, 24 increase autophagy flux. Herein, we highlight CCT020312 as a mammalian target of rapamycin (mTOR) inhibitor-independent autophagy activator, which should function without suppressing the immune response. CCT020312 dose-dependently reduces cytotoxic axonal mutant prion protein aggregate levels within endosomes of primary murine hippocampal neurons and normalizes axonal trafficking deficiencies. Moreover, CCT020312 robustly clears phosphorylated insoluble tau, while reducing tau-mediated neuronal stress vulnerability in patient-derived neuronal models. CCT020312 also restores lysosomal function in neurons differentiated from sporadic Alzheimer's patients fibroblasts bearing epigenetic marks of aging. Taken together, we describe a promising strategy to uncover novel pharmacological agents that normalize cellular neurodegenerative disease pathology.

Running title: Autophagy Activation Normalizes Neurodegeneration Phenotypes

Introduction

Autophagy is a lysosome-mediated molecular recycling pathway, critical for maintaining cellular homeostasis and resilience in response to diverse stresses (Figure 1A).(Ichimura et al., 2000; Kabeya et al., 2000; Tsukada and Ohsumi, 1993) Autophagy functions to degrade potentially damaging species, including infectious pathogens, impaired organelles, (Goodall et al., 2022; Lazarou et al., 2015; Novak et al., 2010) and aggregated proteins. (Kirkin et al., 2009; Ravikumar et al., 2002; Sarraf et al., 2020) Autophagy also degrades superfluous macromolecules including proteins, nucleic acids, carbohydrates, lipids (Lapierre et al., 2013; Singh et al., 2009) and assemblies thereof, (An and Harper, 2018) as well as cellular organelles.(An et al., 2019; Eapen et al., 2021; Jin and Youle, 2012; Khaminets et al., 2015) Within a cell, autophagy occurs at a basal level and can be upregulated in response to numerous stimuli, including stress, serum starvation, or inhibition of mTOR complex 1 (mTORC1), a central regulatory hub.

Autophagy, mediated by proteins encoded by the *ATG* genes, initiates with double membrane or phagophore-mediated sequestration of substrates for degradation (Figure 1A).(Kabeya *et al.*, 2000; Tsukada and Ohsumi, 1993) The phagophore to autophagosome maturation results in double membrane isolation of the degradation substrates. The autophagosome is then trafficked to a lysosome and subsequent fusion yields the autolysosome, wherein acidic lysosomal hydrolases degrade the substrates (Figure 1A).

Naturally occurring mutations in proteins associated with autophagy have revealed a crucial role for autophagy in preventing neurodegeneration during aging; findings that have been robustly validated in murine models.(Alquezar et al., 2021; Bourdenx et al., 2021; Brady et al., 2013; Bucci et al., 2000; Butlers et al., 2019; Chang et al., 2014; Cherry et al., 2013; Clayton et al., 2015; Cotman et al., 2013; Freischmidt et al., 2015; Hara et al., 2006; Harold et al., 2009; Jiang et al., 2019; Jin and Youle, 2012; Kao et al., 2017; Komatsu et al., 2006; Lai et al., 2009; Lee et al., 2022; Lee et al., 2010; Metzger et al., 2010; Oakes et al., 2017; Ochaba et al., 2014; Papassotiropoulos et al., 2000; Ramirez

et al., 2006; Rubinsztein et al., 2011; Sarraf *et al.*, 2020; Sidransky et al., 2009; Tian et al., 2013; von Kleist et al., 2019; Wan et al., 2020; Watanabe et al., 2016; Yang et al., 2014; Yang et al., 2001; Zavodszky et al., 2014) During aging, the efficiency of autophagy can decline for genetic and/or environmental reasons, leading to the detrimental accumulation of protein aggregates and/or damaged organelles, and thereby predisposing an individual to degenerative phenotypes.(Hou et al., 2019) Conversely, studies in model organisms have correlated enhanced autophagic flux to increased healthspan and lifespan.(Fernández Á et al., 2018; Pyo et al., 2013) Thus, pharmacological activation of autophagy represents a promising strategy for ameliorating degenerative diseases that lead to deterioration of the peripheral and central nervous systems (Duan et al., 2021; Lee *et al.*, 2022; Meléndez et al., 2003; Nixon, 2013; Rubinsztein et al., 2012; Rubinsztein et al., 2007; Silva et al., 2020) and linked inflammatory processes that appear to contribute to neurodegeneration. (Crother et al., 2019; Podlesny-Drabiniok et al., 2020; Wang et al., 2021; Zhong et al., 2016)

Numerous efforts have been undertaken to identify small-molecule autophagy activators.(Kaizuka et al., 2016; Lipinski et al., 2010; Zhang et al., 2007) Pharmacological activation of autophagy has been studied most often using the natural product rapamycin, an inhibitor of mTORC1, as well as more potent second generation mTORC1 inhibitors.(Balgi et al., 2009; Chauhan et al., 2015; Chin et al., 2022; Kaizuka *et al.*, 2016; Lipinski *et al.*, 2010; Zhang *et al.*, 2007) (Silva *et al.*, 2020) However, in addition to being a master regulator of autophagy, mTORC1 is a major signaling hub with roles in growth, metabolism and immune function.(Laplante and Sabatini, 2012; Sarkar et al., 2009; Saxton and Sabatini, 2017) Thus, mTORC1-mediated autophagy activation thus suffers from the risk of on-target mechanism-based side effects, including immunosuppression, an undesirable risk for the aged Alzheimer's disease and related dementia populations. Thus, we sought mTORC1 inhibition-independent autophagy activators to complement the progress made in generating potent and selective mTORC1 inhibitors, which are under clinical evaluation.(Renna et al., 2013) A genome-wide siRNA screen revealed that multiple mTORC1-independent signaling pathways exist to regulate autophagy under normal nutritional conditions, further

motivating us to seek pharmacological mTOR inhibition-independent autophagy activators to accelerate lysosomal flux. (Lipinski *et al.*, 2010) There are a few reported mTORC1-independent autophagy activators, however these haven't been systematically evaluated.(Lee et al., 2013; Sarkar et al., 2007a; Sarkar et al., 2007b; Williams et al., 2008)

Prior cell-based screening efforts to identify small-molecule autophagy activators are associated with modest throughput and most often exploited increased autophagosomal localization of the fluorescently labeled autophagy effector LC3-II. (Kaizuka *et al.*, 2016; Lipinski *et al.*, 2010; Zhang *et al.*, 2007) LC3 is expressed cytosolically (termed LC3-I), and upon autophagy initiation it is proteolytically processed and lipidated to afford LC3-II, which localizes to the autophagosome double membrane (Figure 1A). LC3-II remains associated with the autophagosome until its degradation by lysosomal proteases upon formation of the autolysosome. These dynamic changes can be visualized both by immunoblot and by imaging of fluorescently labeled LC3 proteins that undergo a transition from cytosolic distribution to autophagosome-localized puncta (Klionsky et al., 2016). The largest autophagy activator screen reported to date explored 200,000 small molecule candidates. A key limitation of LC3-based approaches is that both activation and inhibition of autophagy increase the cellular abundance of LC3-II, either by inducing the aforementioned maturation of LC3-I into -II or by inhibiting degradation and recycling of autophagosomes and lysosomes leading to LC3-II accumulation.

We envisioned that a complementary screening approach to discover autophagy activators would be to shift the focus away from protein effectors of autophagy to monitoring successful degradation of an autophagy substrate. Lipid droplets were selected as the autophagy substrate for our screen because they were established to be degraded by macroautophagy (Singh *et al.*, 2009). Exposure of cells to fatty acids results in their conversion into triacylglycerides, which accumulate within the ER bilayer and are assembled by a biological pathway into intracellular lipid droplets enclosed in a single monolayer of phospholipids.(Martin and Parton, 2006; Murphy, 2001). Lipid droplets are

dynamic, ubiquitous cellular organelles that serve as critical hubs regulating cellular lipid and energy metabolism. (Olzmann and Carvalho, 2019; Renne and Hariri, 2021; Walther et al., 2017) Mobilization of stored lipids from lipid droplets occurs primarily by lipolysis, mediated via lipid droplet-associated cytosolic lipases such as adipose triglyceride lipase (Lass et al., 2006) and by lipophagy, in which lipid droplets are delivered to lysosomes via macroautophagy and degraded by the lysosomal acid lipase. (Cingolani and Czaja, 2016; Singh *et al.*, 2009) The resulting fatty acids can be utilized by mitochondria and peroxisomes for energy production through β-oxidation. (Olzmann and Carvalho, 2019; Roberts and Olzmann, 2020) The lipid droplet screen is thus expected to identify small molecules that clear lipid droplets by autophagic as well as non-autophagy pathways.

The potential for discovering autophagy activators by monitoring intracellular lipid droplet clearance was first demonstrated in a HeLa cell-based high content imaging screen of 1400 small molecules, which identified one mTORC1-independent autophagy activator that is structurally similar to tamoxifen (vide infra), P29A03.(Lee *et al.*, 2013) This pilot screen used endogenous lipid droplet levels. Inspired by this screen, we decided to increase the basal lipid droplet abundance in our cell-based screen by supplementing the cell growth media with oleic acid, thereby increasing the dynamic range of the lipid droplet clearance assay enabling facile identification of autophagy activators. The kinetics of lipid droplet degradation can be quantified using fluorogenic small molecules, such as BODIPY 493/503, that localize to the hydrophobic environment of lipid droplets, and as a result of the environmental change become fluorescent. (Grandl and Schmitz, 2010; Kim et al., 2012; Lee *et al.*, 2013; Yang *et al.*, 2014)

We describe the optimization, miniaturization, and execution of a high content imaging-based high throughput screen assessing 940,000 small molecules to identify candidates capable of accelerating cellular lipid droplet clearance. After counter-screening, 221 hits emerged and, after manual curation, 120 prioritized hits were tested for their ability to hasten autophagic flux by employing a GFP-LC3-RFP-LC3ΔG ratiometric imaging reporter in RPE1 cells (the 120 include the 77 compounds exhibiting validated enhanced lipid droplet clearance). Of these, 24 were obvious autophagy

activators.(Kaizuka *et al.*, 2016) Numerous additional autophagy assays were conducted on subsets of the 120 hits of interest, including automated microscopy imaging featuring transfected photo-switchable LC3-Dendra2. This kinetic assay revealed that **CCT020312** dose-dependently hastened lysosomal flux in primary cortical neurons, doubling the rate at a **CCT020312** concentration of 500 nM. We demonstrate the potential value of **CCT020312** in restoring neuronal function/viability in multiple cellular models of neurodegeneration phenotypes. **CCT020312** treatment of primary murine hippocampal neurons at concentrations above 50 nM cleared cytotoxic axonal endosome-delimited aggregates of a mutant prion (PrP) protein (PrP^{PG14}), while restoring axonal vesicular trafficking capacity. In addition, **CCT020312** robustly reduced phosphorylated and insoluble tau in a human induced pluripotent stem cell (iPSC)-derived neuronal familial tauopathy model, while reducing tau-mediated neuronal stress vulnerability. Lastly, **CCT020312** activated autophagy in direct-differentiated sporadic Alzheimer's disease (AD) neurons harboring epigenetic marks of aging, normalizing lysosomal function as well as reduced Aβ levels in sporadic and PSEN1 mutant AD directly induced neurons. Together these data demonstrate the potential of using **CCT020312** in elderly dementia patients to slow disease progression.

Results

Lipid droplet clearance as a basis for discovering autophagic flux activators

A major lipid metabolism mechanism in cells is the degradation of lipid droplets by autophagy (Fig. 1A) (Singh *et al.*, 2009). Prior studies show that pharmacological inhibition of autophagy increases cellular lipid droplet load, whereas pharmacological autophagy activation by the mTORC1-inhibitor rapamycin decreases lipid droplet quantities and triacyl glyceride levels (Singh *et al.*, 2009). Inspired by previous work by (Lee *et al.*, 2013), we set out to enhance the sensitivity of this substrate degradation assay by increasing lipid droplet load in the cell by oleic acid supplementation, while enhancing throughput to be able to screen much larger small molecule libraries than previously possible in autophagy activator discovery programs (Fig. 1B).

Human SW1990 adenocarcinoma cells were chosen for their large size, uniform growth patterns, and adherent properties that facilitate image-based analysis of cellular lipid load. SW1990 cells were plated in standard complete growth medium supplemented with 10 μM oleic acid complexed to bovine serum albumin (BSA) and allowed to adhere for ≈ 24 h. Notably, this screen was carried out in rich media in order to discover compounds able to activate autophagy without being confounded by nutrient starvation. Supplementing the cell culture medium with 10 μM oleic acid does not activate autophagy by itself, as evidenced by the lack of RFP/GFP ratio change in HeLa RFP-GFP-LC3 cells (Kimura et al., 2007) and the absence of gene level changes in HEK293T cells by RNA-Seq (Supplemental Figure 1A).

For assay validation, cells were treated with a small test panel of known autophagy activators, including the mTORC1 inhibitor rapamycin, the class 1A phosphatidylinositide 3 kinase / mTORC1 / mTORC2 inhibitor PI-103, mTORC1 / mTORC2 dual inhibitor torkinib (PP242), and the G-protein coupled estrogen receptor agonist tamoxifen (Supplemental Figure 1B). Following compound treatment for 24 hours, cells were fixed, stained and then imaged for cellular lipid abundance. A semi-automated image analysis pipeline was set up and optimized to identify hit compounds that decrease lipid droplet content (see M&M for details). This image quantification pipeline was used to analyze the impact of our test panel of autophagy inducers on lipid droplet levels and, as expected, could detect significant acceleration of lipid droplet clearance in SW1990 cells (Supplemental Figure 1C). Having settled on the optimized small molecule candidate treatment time of 20 hours, we treated three other human cancer cell lines with the aforementioned known autophagy activators and found that they induced decreases in cellular lipid droplet area in all cell lines tested (Supplemental Figure 1B). We then correlated lipid droplet clearance with a classical autophagy marker: conversion of cytosolic LC3-I to lipidated LC3-II.(Klionsky et al., 2021) A correlation exists between lipid droplet clearance and autophagy induction (Supplemental Figure 1D), indicating that our lipid droplet-based assay is suitable to identify autophagy inducers.

A Pilot screen verified reproducibility and feasibility of the optimized lipid droplet clearance assay

To validate the lipid droplet clearance assay and confirm feasibility for a high-throughput screen, we first assessed a collection of 1280 annotated bioactive small-molecules, the Library of Pharmacologically Active Compounds (LOPAC) (https://www.sigmaaldrich.com/US/en/product/sigma/lo1280). Following the protocol described in the materials and methods section and outlined in Fig. 1B, SW1990 cells were plated in 1536-well plates in oleic acid supplemented standard complete growth, allowed to accumulate lipid droplets over 24 hours, and then treated with the LOPAC library compounds at a concentration of 4 μM for 20 hours. Hits were identified as compounds that reduced the total cellular lipid droplet area by >50% relative to DMSO in a non-cytotoxic manner (i.e. there was < a 30 % reduction in cell number). This 1536-well LOPAC screen was performed three times, with 59% of the hits being confirmed in at least 2 of the 3 screened plates (Supplemental Figure 1E, 1F), validating the robustness of the screening setup.

With the lipid droplet clearance assay validated and miniaturized, we proceeded to screen ~940,000 compounds in singlet at 5 μM (Figure 1C). A total of 7105 primary hit compounds were identified. These primary hits were re-assessed in triplicate, with 729 hits being confirmed. Hits were further assessed for non-cytotoxic dose-dependent reduction in cellular lipid load (concentration range: 0.1 μM - 10 μM). Small molecules achieving a > 50 % reduction in total lipid area and a ≤ 30 % reduction in cell number at the maximum nontoxic dose afforded 409 hits being subjected to counter-screening.

Next, a counterscreen was performed to identify and remove compounds that cause significant quenching of BODIPY 493/503 fluorescence in fixed cells where autophagy is not possible. This approach identifies hits that are false positives because they simply quench BODIPY 493/503 fluorescence (see Materials & Methods for more details). This approach eliminated 188 false positive hits that quenched the BODIPY 493/503 fluorescence, rather than reducing cellular lipid load. The remaining 221 hit

compounds were manually curated by an experienced medicinal chemist (H.M.P.), who eliminated pan-assay interference compounds, compounds bearing significant metabolic liabilities, and compounds than were often hits in multiple unrelated high-throughput screens. This effort yielded 108 compounds, of which 81 were commercially available.

To identify compounds acting because of genetic alterations only present in certain cancer cells, the 81 reordered compounds were analyzed for their ability to hasten lipid droplet clearance in three different immortalized cancer cell lines, including the original screening adenocarcinoma cell line, SW1990, the fibrosarcoma cell line HT-1080, and the glioblastoma cell line U251 (Supplemental Fig1F). We deprioritized those hits displaying activity in only one cell line. The vast majority, 77 compounds, enhanced lipid droplet clearance in at least two out of the three cell lines (Figure 1D). These validated hit compounds represent pharmacologic agents capable of decreasing lipid droplet levels in a variety of cell types by a variety of mechanisms.

Enhancers of lipid droplet clearance activate general autophagy flux

In order to identify the subset of hit compounds that were accelerating lipid droplet clearance through activation of autophagy, we made use of the well-established autophagy flux reporter GFP-LC3-RFP-LC3ΔG (Kaizuka *et al.*, 2016) in RPE1 cells. The probe is cut by the endogenous cellular protease ATG4 and the GFP-LC3 portion of the reporter becomes lipidated and localizes to the autophagosome upon autophagy induction. Therefore, the GFP moiety is first rapidly quenched in the low-pH environment of the autolysosome and subsequently degraded together with the rest of the autophagosomal substrates. The RFP-LC3ΔG cleavage product remains cytosolic due to a missing *C*-terminal glycine, critical for the enzymatic lipidation of LC3. As such, altered GFP/RFP intensity ratio corresponds to a change in autophagy flux, as GFP-LC3 and RPF-LC3ΔG are produced at equal levels. High autophagy flux will result in low levels of GFP-LC3 (faster turnover) and therefore a low GFP/RFP ratio. We used a polyclonal, FACS-sorted RPE1 cell line stably expressing the GFP-LC3-RFP-LC3ΔG reporter to follow changes in autophagy flux upon compound treatment. Since compounds may act

early or late, we subjected reporter cells to live-cell imaging to allow a kinetic analysis over a period of 72 hours. 120 compounds including the 77 compounds validated for enhanced lipid droplet clearance were tested in triplicate and at three different concentrations: 50 nM, 500 nM, and 5 μM (Figure 1E). Images in the green, red, and phase channel were taken every 2h on an Incucyte S3 and analyzed for total integrated intensity (green, red) and cell confluency (phase). Hits were defined as compounds causing a ≥20 % increase in autophagy flux over ≥ 12h treatment (Supplemental Figure 1I; for details see M&M), resulting in 62 primary hits. To further determine whether compounds caused long-term effects or shifted steady state levels (Supplemental Figure 1J), we also analyzed the slope of autophagy flux changes over time in comparison to DMSO (Figure 1F). About half of the compounds passed this hit criteria (Supplemental Figure 1K). Those included compounds causing rapid induction as well as compounds acting at later time points–hours or days after treatment in some cases (Figure 1E). Based on compound availability, 35 primary hits were re-analyzed in a dose-dependent fashion employing12-dilutions (50nM – 10μM; 24 secondary hits) and subsequently categorized based on their autophagy flux pattern over time (Supplemental Figure 1L,M).

Lipid droplet screening hits known to be autophagy activators

One risk associated with carrying out a HTS screen for compounds accelerating lipid droplet clearance is that the majority of hits would act through mechanisms specific to lipids, and we would not identify hits that accelerated the degradation of proteins, nucleic acids, carbohydrates, and assemblies thereof, (An and Harper, 2018) as well as cellular organelles.(Eapen *et al.*, 2021) However, several of the 40 hit compounds shown to activate the autophagy reporter corresponded to previously identified, validated autophagy activators, including the mTor inhibitors rapamycin, Torin-1 and PI-103,(Park et al., 2008), and MP7,a previously identified PDK1 inhibitor,(Daniele et al., 2017) as well as fluspirilene, one of a number of previously identified antipsychotic compounds known to activate autophagy.(Petcherski et al., 2019; Varalda et al., 2020; Xia et al., 2010; Zhang *et al.*, 2007)

Identification of novel small-molecule autophagy activator CCT020312

We selected hit compound **CCT020312** for further analysis due to its top quartile activity in the lipid droplet clearance assay in all the cell lines evaluated and because we identified a structurally analogous compound, C48 (ANP990) with similar activity in clearing lipid droplets (Figure 2A). **CCT020312** consistently clears lipid droplets at low single digit μM doses (Figures 2B,C; Supplemental Figure 1G), while CellTiter-Glo luminescent cell viability assay reveals no toxicity in SW1990 and U251 cells at doses below 10μM (Supplemental Figure 2A). **CCT020312** also induced autophagic flux in RPE1 cells stably expressing the GFP-LC3-RFP-LC3ΔG reporter, at concentrations below 2 μM (Figure 2D, Supplemental Figure 2B). Cell toxicity with this non-cancerous cell line was noticeable already at concentrations ≥ 3μM (Figure 2E). Analog C48 (ANP990) also induced autophagic flux in RPE1 cells stably expressing the GFP-LC3-RFP-LC3ΔG reporter (Supplemental Figures 2C and 2D).

To further differentiate between targeted autophagy induction versus an induced stress response caused by compound toxicity, we compared the autophagy flux induction caused by CCT020312 to a structurally related, yet inactive compound carboxy CCT (Figure 2A). The difference in autophagy flux induction between active and inactive compound was apparent at concentrations ≥ 0.5 μM with increasing significance (Figure 2F). Further evidence that **CCT020312** was inducing autophagy in a targeted manner came from the classical lipidation assay of LC3B in HeLa cells (Klionsky *et al.*, 2021). While CCT020312 induced lipidation of LC3B in a dose-dependent manner, inactive carboxy CCT did not (Figure 2G). HeLa cells treated for 20 hours with **CCT020312** formed more LC3 puncta and these puncta colocalized with LAMP2, suggesting more autolysosomes (Supplemental Figure 2E).

CCT020312 Resynthesis and Characterization

We then chose to scale up synthesis of **CCT020312** so that we would be able to have enough material for use in multiple downstream biological assays. **CCT020312** was synthetized using a modified method following literature procedure (Supplemental

Scheme 1).(Stockwell et al., 2012) Final preparative high-performance liquid chromatography purification yielded 600 mg of **CCT020312** in 92% yield (Supplemental Figure XX). All subsequent biology assays were performed with this resynthesized material.

We performed dynamic light scattering experiments on **CCT020312** in deionized water and in PBS to further characterize its proclivity foe self-assembly. DOPC unilamellar liposomes were used as the positive control – as a homogeneous population can be achieved by extruding DOPC lipids through a mini-extruder using a pore size of 200 nm – and water was used as the negative control (Supplemental Figure XXA Colloid). In deionized water, **CCT020312** forms colloids with a colloid diameter of ~200 nm at 1 μM, 10 μM and 50 μM (Supplemental Figure XXB Colloid). In PBS, **CCT020312** has a CAC around 10 μM with a colloid diameter at ~79 nm and forms larger colloids and aggregates at 50 μM (Supplemental Figure XXC Colloid). All subsequent experiments were performed with concentrations of **CCT020312** no higher than 10 μM.

CCT020312 increases autophagic flux in primary mouse cortical neurons

To provide additional evidence for accelerated dose-dependent autophagic flux after **CCT020312** treatment, an optical pulse labeling assay was performed employing a fusion between the autophagy effector protein LC3 and the photoswitchable fluorescent sensor protein Dendra2. Primary mouse cortical neurons were transfected with LC3-Dendra2 and subsequently irradiated with 405 nm light to irreversibly convert Dendra2 emission from green to red fluorescence (Figure 2H, bottom left). Xxx individual transfected neurons were monitored longitudinally by automated microscopy to quantify the rate of decrease in red fluorescence over time, allowing a determination of the half-life of the photoconverted LC3 protein upon **CCT020312** treatment (Figure 2H, top).(Sharma et al., 2012) We observe dose-dependent reduction in mean half-life of LC3-Dendra2 upon **CCT020312** treatment, consistent with activation of autophagic flux by this compound (Figure 2H, bottom right). In contrast, the inactive control compound carboxy-CCT does not accelerate LC3-Dendra2 degradation upon treatment.

CCT020312 increases autophagic flux in human iPSC-derived cortical neurons

We next tested the activity of **CCT020312** in human iPSCs that were differentiated into cortical neurons. A 24-hour treatment of **CCT020312** resulted in a significant increase of lysosomal activity, even at concentrations as low as 50 nM, as measured by DALGreen/DAPRed and Lysotracker fluorescence area per cell (Figures 2I, 2J Supplemental Figures 2F, 2G). DALGreen and DAPRed are two amphiphilic fluorescent probes, which mimic intramembrane phospholipids, and become incorporated into the growing phagophore. DALGreen and DAPRed are designed to monitor autophagic flux by preferentially labeling autolysosomes or the entire autophagic process (autophagosomes and autolysosomes), respectively.(Iwashita et al., 2018) Both probes are incorporated into non-mature autophagosome membranes partly because of their fluorogenic 1,8-naphthalimide scaffold. DALGreen fluorescence in addition to its hydrophobicity is enhanced by acidic pH, which occurs after the autophagosome fuses with the lysosome. In contrast, DAPRed fluorescence is not affected by pH and therefore measures total autophagosomes plus autolysosomes. After 24 hour treatment of human iPSC-derived cortical neurons with CCT020312, DALGreen and DAPRed are added for 1 hour. Relative to DMSO-treated neurons, neurons treated with CCT020312 exhibited dose-dependent increase in induction of autophagy (increase in DAPRed fluorescence area) and in autophagic flux (increase in ratio of green/red fluorescence area), as this represents greater number of autolysosomes forming relative to the number of autophagosomes forming. LysoTracker Red fluoresces only in acidic environments such as lysosomes and increased fluorescence intensity suggest larger and/or greater number of lysosomes in CCT020312-treated neurons. Together, these results are consistent with the notion that CCT020312 treatment enhances autophagic flux in human iPSC-derived cortical neurons.

CCT020312 increases TFEB nuclear localization without inhibiting mTORC1

To begin investigating the mechanism by which **CCT02312** activates autophagy, transcription factor EB (TFEB) nuclear localization was assessed after **CCT02312** treatment in HeLa cells. TFEB is regarded as a master regulator of lysosomal biogenesis and autophagic function. Upon autophagy activation, TFEB is dephosphorylated by calmodulin-dependent calcineurin at Ser142 and Ser211, which results in its translocation from the lysosomal surface to the nucleus where TFEB initiates transcription of genes involved in lysosomal biogenesis and autophagy.(Sardiello et al., 2009; Settembre et al., 2011) Immunofluorescence of TFEB in HeLa cells treated with 1 μM **CCT020312** is associated with a ~70% increase on average in nuclear translocation of TFEB compared to vehicle treatment (Figure 3A).

TFEB nuclear translocation can be negatively regulated by phosphorylation of its Ser 142 and Ser 211 residues by the mammalian target of rapamycin complex 1 (mTORC1) (Martina et al., 2012; Roczniak-Ferguson et al., 2012; Settembre et al., 2012) In an effort to determine whether **CCT020312** inhibits mTORC1, thereby leading to TFEB nuclear translocation, we assessed the phosphorylation state of TFEB at Ser 211 via immunoblotting (Figure 3B). Treatment of HeLa cells for 20 hours with positive control 250 nM Torin-1 led to statistically significant reduction of p-TFEB (S211) but 1 μM **CCT020312** treatment did not change p-TFEB (S211) levels. It has been reported that other phosphorylation sites of TFEB (perhaps regulated by other kinases) may modulate its activity, and some of these are via mTOR-independent mechanisms of action.(Vega-Rubin-de-Celis et al., 2017) In the absence of antibodies for these phosphorylation sites, however, we do not know if **CCT020312** treatment affects their levels.

Intrigued by this initial result, we decided to more directly probe whether **CCT020312** alters mTORC1 signaling by interrogating the phosphorylation state of other downstream substrates: p70S6 kinase 1 (S6K) at Thr 389, mammalian autophagy-initiating kinase ULK1 at Ser 757 and eukaryotic translation initiation factor 4E-binding protein 1 (4E-BP1) at Thr 37/Thr46 or Ser 65 in HeLa and U251 cells (Figures 3C, 3D, 3E, 3F, 3G, 3H). Most of the existing literature on pharmacological autophagy activation involves mTORC1 inhibition (e.g. Torin-1 and rapamycin) (Kim et al., 2011; Kim and Guan,

2015; Noda and Ohsumi, 1998; Thoreen et al., 2009), and we wanted to assess whether **CCT020312** followed a similar mechanism. S6K and 4E-BP1 are key regulators for mRNA translation activation (Gingras et al., 2001; Sengupta et al., 2010; Wang et al., 2005) and ULK1 is hyperphosphorylated during high mTOR activity to prevent autophagy activation (Kim *et al.*, 2011). In contrast to 250 nM Torin-1 treatment for 20 hours, **CCT020312** did not change any mTORC1 substrates' phosphorylation levels in HeLa cells or U251 cells (Figures 3C, 3D, 3E, 3F, 3G, 3H).

CCT020312 increases TFEB nuclear localization without inhibiting mTORC1

To begin investigating the mechanism by which **CCT02312** activates autophagy, transcription factor EB (TFEB) nuclear localization was assessed after **CCT02312** treatment in HeLa cells. TFEB is regarded as a master regulator of lysosomal biogenesis and autophagic function. Upon autophagy activation, TFEB is dephosphorylated by calmodulin-dependent calcineurin at Ser 142 and Ser 211, which results in its translocation from the lysosomal surface to the nucleus where it initiates transcription of genes involved in lysosomal biogenesis and autophagy.(Al-Bari and Xu, 2020; Sardiello *et al.*, 2009; Settembre *et al.*, 2011) Immunofluorescence of TFEB in HeLa cells treated with 1 μM **CCT020312** reveals a ~70% increase in nuclear translocation of TFEB on average compared to vehicle treatment (Figure 3A).

TFEB nuclear translocation can be negatively regulated by phosphorylation of its Ser 142 and Ser 211 residues by the mammalian target of rapamycin complex 1 (mTORC1).(Martina *et al.*, 2012; Roczniak-Ferguson *et al.*, 2012; Settembre *et al.*, 2012) In an effort to determine whether **CCT020312** inhibits mTORC1, thereby leading to TFEB nuclear translocation, we assessed the phosphorylation state of TFEB at Ser 211 via immunoblotting (Figure 3B). Treatment of HeLa cells for 20 hours with positive control 250 nM Torin-1 led to statistically significant reduction of p-TFEB (S211) but 1 μM **CCT020312** treatment did not change p-TFEB (S211) levels. It has been reported that other phosphorylation sites of TFEB (perhaps regulated by other kinases) may modulate its activity, and some of these are via mTOR-independent mechanisms of action.(Vega-

Rubin-de-Celis *et al.*, 2017) (Li et al., 2016) In the absence of antibodies for these phosphorylation sites, we do not know if **CCT020312** treatment affects their levels.

Since we did not detect a reduction in the phosphorylation level of TFEB at Ser 211, to determine whether **CCT020312** can act without directly inhibiting mTORC1 signaling, we interrogated the phosphorylation state of other mTORC1 downstream substrates. We measured the phosphorylation levels of p70S6 kinase 1 (S6K) at Thr 389, mammalian autophagy-initiating kinase ULK1 at Ser 757 and eukaryotic translation initiation factor 4E-binding protein 1 (4E-BP1) at Thr 37/Thr46 or Ser 65 in HeLa and U251 cells (Figures 3C, 3D, 3E, 3F, 3G, 3H). Most of the existing literature on pharmacological autophagy activation involves mTORC1 inhibition (e.g. Torin-1 and rapamycin),(Kim *et al.*, 2011; Kim and Guan, 2015; Noda and Ohsumi, 1998; Thoreen *et al.*, 2009) and we wanted to assess whether **CCT020312** utilized a similar mechanism. S6K and 4E-BP1 are key regulators for mRNA translation activation(Gingras *et al.*, 2001; Ma and Blenis, 2009; Sengupta *et al.*, 2010; Wang et al., 2010) and ULK1 is hyperphosphorylated during high mTOR activity to prevent autophagy activation.(Kim *et al.*, 2011) In contrast to the result achieved with 250 nM Torin-1 treatment for 20 hours, **CCT020312** did not change any mTORC1 substrates' phosphorylation levels in HeLa cells or U251 cells (Figures 3C, 3D, 3E, 3F, 3G, 3H).

TFEB controls genes that belong to the Coordinate Lysosomal Expression and Regulation (CLEAR) network.(Palmieri et al., 2011) To find out if **CCT020312** treatment induces TFEB nuclear localization to activate its transcription activity, we performed RNA-Seq analysis of HeLa and HEK293T cells treated with 1 μM **CCT020312** for 20 hours. **CCT020312** treatment displayed a robust change towards the CLEAR transcriptomic program, as we detected 1292 genes were significantly upregulated and 1501 genes were significantly downregulated when compared to vehicle in HEK293T cells. This corresponded to approximately 17% of total genes (Figure 4A and Supplemental Table 3). We next searched among these significant differentially expressed genes for known TFEB mediated genes which include autophagy and lipid metabolism related genes. Of these 603 compiled genes shown to be regulated by TFEB,(Palmieri *et al.*, 2011; Sardiello *et al.*, 2009; Settembre *et al.*, 2011; Settembre et al., 2013) we detected 103 of these genes' whose expression is significantly changed after **CCT020312** treatment in

HEK293T cells and 114 of these genes exhibited changes in HeLa cells. These genes include known autophagy genes *ATP6V0C*, *CTSD*, *VPS18*, and *SQSTM1*, which we detected to be upregulated. In addition, gene set enrichment analysis shows that other stress response signaling pathways are not preferentially upregulated, suggesting that TFEB gene activation is independent of a stress response (Figure 4B). These results suggest **CCT020312** might be inducing autophagy via activating an autophagy-related transcriptomic program.

Lipidomics analysis of time-course treatment with autophagy activators

There are numerous modes of crosstalk between autophagy and lipid metabolism. For example there are direct interactions with lipids and the autophagic machinery, as in the case of the signaling cascades modulating mTORC1 (e.g. PI(3,4,5)P3 activating the Akt signaling pathway). Moreover, the recruitment of LC3 to the membrane by attachment of phosphatidylethanolamine to generate LC3-II and PI3P is another example. However, in addition to these direct interactions there is also lipid remodeling, which influences the physicochemical properties of lipid bilayers (e.g. fluidity and phase transitions). Moreover, autophagy not only degrades lipids in catabolic processes, but also initiates lipid synthesis and remodeling in a time dependent manner to support hastened autophagy from a basal state. Because this phenomenon is most likely cell type specific and to some extent dependent on the type of autophagy induced, we sought to make general observations of how the lipidome temporally changes in response to autophagy induction via rapamycin or **CCT020312** treatment. Intriguingly, we observe overall trends in several lipid classes that may be fundamental to autophagy regardless of whether the mechanism is mTOR dependent or not. At two hours post treatment, there is an increase of phosphatidyethanolamines (PE), phosphatidylcholines (PC), phosphatidylserines (PS) and sterols (SL) (Figure 4C). This is most likely associated with de novo lipid synthesis to support the membrane requirements for accelerated lysosomal flux.(Ichimura *et al.*, 2000) This is followed by the catabolic decrease in diacylglycerides (DAG) and triacylglycerides (TAG) at the 12 and 24 hour time points. At these time points the autophagic pathway switches from a state of lipid synthesis to predominantly lipid degradation. At these later time points we observe a slight decrease of total phospholipids and a large decrease of

DAG and TAG, which are known substrates of autophagy. The latter is the predominate neutral lipid comprising lipid droplets. Overall, throughout the autophagy process ceramides (CE) stayed elevated, possibly eliciting autophagy through its own means of regulation, as CE can induce autophagy on its own through nutrient regulation and UPR signaling. Overall lipidomics analysis reveals that **CCT020312** modulates the lipidome similarly to rapamycin over a time course (Figure 4C).

Proteomics analysis of HEK293T cells treated with CCT020312

Proteomics analysis of HEK293T cells treated with CCT020312 (24 hours with 500 nM), 1 μM CCT020312 and 2.5 μM CCT020312 reveals significant downregulation of proteins related to mitochondria and mitochondrial processes (Figure 4E). This is in contrast to 250 nM rapamycin treatment, which downregulated membrane transport proteins (Figure 4D). Proteins that exhibited a strong dose response upon CCT020312 treatment include NDFIP1, PIK3C2B and CLU. NDFIP1 has been linked to mTORC1 signaling in the literature,(Layman et al., 2017) while CLU is a secreted chaperone that prevents the formation of amyloid from multiple proteins.(Kumita et al., 2007) Phosphoproteomics analysis of the same samples reveals that a phosphopeptide of TAX1BP1 at Ser 344 becomes more abundant as the dose of CCT020312 increases from 1 μM to 2.5 μM (Figure 4G). TAX1BP1 is an autophagy receptor whose phosphorylation has been linked to localization with lysosomes. In addition**,** phosphorylation sites of p70S6K and mTOR were upregulated upon CCT020312 treatment whereas they were downregulated upon rapamycin treatment, providing more evidence for distinct mechanisms of action, and for CCT020312 a mechanism that does not involve mTORC1 inhibition. Further analysis of phosphoproteomics data is ongoing and might uncover the molecular signatures of autophagy activators working independently of mTORC1 inhibition.

CCT020312 does not activate autophagy by stress responsive signaling pathways

Prior literature suggested that **CCT020312** can activate the PERK signaling arm of the unfolded protein response (UPR).(Stockwell *et al.*, 2012) Activation of PERK by the global endoplasmic reticulum stressor tunicamycin has been shown to activate

autophagy.(Luhr et al., 2019) Thus, we initially hypothesized that **CCT020312** induced autophagy via PERK activation. However, at the lower concentrations used in our experiments, **CCT020312** that we synthesized or purchased from commercial sources did not activate PERK as measured by RNA-Seq analysis of PERK-regulated target genes, nor was PERK activated in cells expressing the ATF4-Fluc reporter of PERK activation (**Fig. S3A,B**). Further, cotreatment with the PERK kinase inhibitor GSK2656157(Axten et al., 2013) did not affect lipid droplet clearance induced by **CCT020312** in U251 cells (**Fig. S3C**). Similarly, co-treatment with the PERK signaling inhibitor ISRIB (Sidrauski et al., 2015) did not impact LC3-I to LC3-II conversion in U251 cells (**Fig. S3D**). Also, **CCT020312** failed to affect LC3-I to LC3-II band conversion in *Perk*$^{-/-}$ MEFs, except at the highest dose employed (**Fig. S3E**).

Apart from canonical PERK signaling, **CCT020312** has been suggested to promote protection against proteotoxic insults through PERK-dependent activation of the NRF2-regulated oxidative stress response (OSR).(Ganz et al., 2020) NRF2 activity has also been implicated in the induction of autophagy.(Dodson et al., 2015) This suggests that **CCT020312** could induce autophagy by activating NRF2. However, we did not observe **CCT020312**-dependent induction of NRF2 target genes by RNAseq (**Fig. S3A**) or **CCT020312**-dependent activation of the NRF2-responsive ARE-FLuc reporter in cell-based assays (**Fig. S3F**). In addition, we did not observe activation of either the IRE1/XBP1s or ATF6 signaling arms of the UPR or the HSF1-regulated heat shock response by RNAseq (**Fig. S3A**) or in cells expressing luciferase reporters specific to these three stress-responsive signaling pathways (**Fig. S3G-I**). Collectively, these results indicate that **CCT020312** does not promote autophagy through activation of the three signaling arms of the UPR or other stress-responsive signaling pathways such as the OSR or Heat Shock Response.

CCT020312 was initially discovered in an effort to identify molecules capable of activating the G1/S checkpoint. The authors screened 63,000 small molecules at a concentration of 10 uM for 24 hours to identify small molecules that inhibit pRB phosphorylation for the purpose of cancer cell growth inhibition.(Stockwell *et al.*, 2012)

Since activating the G1/S checkpoint did not occur by the expected pathways, CCT020312 was hypothesized to function as a PERK activator that phosphorylates EIF2α.(Stockwell *et al.*, 2012) In multiple labs we carefully monitored cell growth after CCT020312 treatment and we see no evidence that CCT020312 inhibits cell growth in numerous cancer cell lines, in our RPE1cell line, in primary murine neurons and in iPSC-derived human neurons. CCT020312 was reported to be a PERK activator that phosphorylates EIF2α. We only see evidence for EIF2α phosphorylation at a concentration of 5 μM. Bruch et al. showed that in neurons with 3 repeat Tau overexpression, there was no PERK activation upon 200 nM CCT020312 treatment as evidenced by the lack of EIF2α and NRF2 phosphorylation. (Bruch et al., 2017) CCT020312 when employed at a concentration of 200 nM only increased phospho-NRF2 levels in the presence of the neurotoxin annonacin in 4-repeat Tau neurons, no phospho EIF2α was observed. Treating wild type mice with 2 mg/Kg/day CCT020312 for 6 weeks starting at 9 weeks of age modestly increased phospho PERK and NRF2, not convincing evidence for pharmacodynamic activation of the PERK pathway with CCT020312 either, consistent with our ability to activate autophagy with CCT020312 in *Perk*$^{-/-}$ MEFs.

Axonal endoggresomes reduced by CCT020312 in a familial neuronal prion disease model

Intraneuronal non-native protein aggregates that compromise vesicular trafficking are a common and early feature of many neurodegenerative diseases.(Stokin et al., 2005) Misfolded protein aggregates have been observed to accumulate prominently within dystrophic axons, inside enlarged lysosome-like structures that also contain incompletely digested material.(Lee et al., 2011; Nixon, 2017; Sikorska et al., 2004; Zanusso et al., 2007) Previous work showed that expression of a 14 octapeptide repeat of the human prion protein (PrP^{PG14} ; there are 9 octapeptide repeats in PrP^{WT}) associated with non-transmissible human familial Gerstmann-Sträussler-Scheinker human prion syndrome (GSS) in cultured hippocampal neurons, results in the formation of enlarged endosomes containing PrP^{PG14} aggregates, compared to the small vesicles in axons comprising PrP^{WT}(cf. Figure 5B DMSO left panel to the DMSO right panel).(Chassefeyre et al., 2021)

Expresion of PrP was under control of the mouse PrP promoter (MoPrP),(Borchelt et al., 1996) and contained the mouse endogenous PrP secretory signal sequence (SS) and a C-terminal GPI anchor sequence to ensure proper passage through the secretory pathway.(Chassefeyre *et al.*, 2021)The large PrP^{PG14} membrane-delimited aggregate structures formed inside axons are termed endoggresomes, and they accumulate at dystrophic swollen sites within axons (see DMSO panels in Figure 5B). Endoggresomes form following the active transport of smaller PrP^{PG14}-carrying Golgi-derived vesicles into the axon by their association with the small endolysosomal GTPase Arl8, which recruits kinesin-1 and Vps41(HOPS) onto PrP^{PG14}-carrying endosomes. In the axon, HOPS-mediated homotypic fusion of PrP^{PG14}-containing vesicles generates enlarged aggregate-containing endolysosomes that disrupt calcium dynamics, impair the axonal transport of vesicular cargo, and reduce neuronal viability, and thus appear to be central to inherited prion disease etiology.(Chassefeyre *et al.*, 2021) This so-called axonal rapid endosomal sorting and transport-dependent aggregation (ARESTA) mechanism of endoggresome formation can be inhibited by genetic downregulation of the Arl8b/kinesin-1/Vps41(HOPS) axis, which reduces PrP^{PG14} endoggresomes and restores neuronal heatlh and viability. (Chassefeyre *et al.*, 2021) Importantly, expressing of PrP^{PG14} results in significantly impaired lysosomal clearance capacity in axons, thus endoggresomes form within endolysosomes that do not acidify and are not properly degraded and grow over time (Chassefeyre *et al.*, 2021) Figure 5E).

To determine whether autophagy activation could degrade PrP^{PG14} endoggresomes in axons, primary hippocampal neurons were transfected with PrP^{PG14}-mCherry (mCh) at 7 days in vitro (DIV), treated for 2h with different concentrations of **CCT020312** at 8 DIV, and endoggresome densities were quantified at DIV 9 on fixed samples (Figure 5A). Treatment of neurons with **CCT020312** above a media concentration of 50 nM significantly reduced endoggresome levels in a dose-dependent manner, in axons of neurons expressing PrP^{PG14}-mCh, as indicated by lower densities that were indistinguishable from those of neurons expressing PrP^{WT}-mCh (Figure 5B). Treatment of neurons with **CCT020312** had no effect on PrP^{WT}-mCh normal vesicle densities (Figure 5B). Because axonal PrP^{PG14}-mCh endoggresomes are well-formed by

DIV 8, but densities continue to increase by DIV 9 (Figure 5C), the reduced endoggresome densities observed following treatment with **CCT020312** at DIV 8 indicate that **CCT020312** can efficiently clear endoggresomes from mammalian axons and potentially inhibit their formation as well. As a control, treatment of neurons with the inactive analog carboxy-CCT did not alter PrP^{PG14}-mCh endoggresome densities, while also not influencing PrP^{WT}-mCh vesicle numbers (Figure 5B). To test whether reduced PrP^{PG14}-mCh endoggresome densities were not the result of observational bias from **CCT020312**-mediated toxicity, we quantified neuronal viability using a cell death assay (STAR Methods). Quantification of the percentage of dead neurons at DIV 9 using a Hoechst 33342 (total cell count) and NucGreen Dead (dead cell count), and treated with **CCT020312**, DMSO vehicle control, or with the inactive carboxy-CCT analog following the same treatment paradigm (Figure 5A), indicated that compound concentrations produced similar cell death levels (Supplemental Figure 4B). To test whether activation of degradative pathways by known autophagy activators could reduce PrP^{PG14} axonal aggregates, hippocampal neurons were treated with the established mTORC1 inhibitor rapamycin using the same treatment paradigm. We observed reduced endoggresome burden in neurons expressing PrP^{PG14}-mCh in the presence of rapamycin, while there were no changes in PrP^{WT}-mCh vesicle densities (Supplemental Figure 4A). Altogether, these data highlight the efficacy of compound **CCT020312** and rapamycin in reducing PrP^{PG14}-mCh endoggresomes at low nM concentrations, indicating that activating autophagy is a viable and generalized strategy to clear or inhibit axonal PrP^{PG14} endoggresomes from the axons of mammalian neurons.

CCT020312 reduces mutant prion protein endoggresomes via enhancing endolysosomal acidification

Using LysoTracker in axons transfected with PrP^{WT}-mCh, or PrP^{PG14}-mCh, or untransfected; single-particle quantitation of PrP^{PG14}-mCh particles colocalizaing with FIREpHLy reveals axonal lysosome acidification (Figure 5F)

CCT020312 restores axonal transport in a neuronal prion disease model

In addition to the formation PrP^{PG14} endoggresomes, live imaging revealed the movement of small PrP^{PG14}-mCh vesicles within axons of neurons expressing PrP^{PG14}-mCh (Figure 5A). Semi-autonated single-particle high-resolution quatitative image analysis (Neumann et al., 2017) showed impaired movement of PrP^{PG14}-mCh (+ DMSO vehicle) vesicles 2 days post-transfection, as after entering the axon, the majority of PrP^{PG14}-mCh vesicles remained stationary compared to those moving in axons of neurons expressing PrP^{WT}-mCh (+ DMSO vehicle) (Figure 5C, Supplemental Figure 5A, Supplemental Movies 1 and 2). The remaining moving PrP^{PG14}-mCh vesicles also displayed defective movement compared to that of PrP^{WT}-mCh vesicles, as they spent less time in motion, and paused more frequently during runs (Figure 5B). Moreover, PrP^{PG14}-mCh vesicles moved significantly slower and their movement was less processive, as indicated by decreased velocity and run length cumulative distribution functions (CDFs), respectively (Figure 5C). Notably, treatment of neurons with **CCT020312** above a media concentration of 50 nM resulted in a signficant rescue of most transport defects phenocopying the transport observed for PrP^{WT}-mCh vesicles (Figure 5C-D; Supplemental Movie 3). In the case of anterograde segmental velocities, treatment with **CCT020312** moreover enhanced the speed of PrP^{PG14}-mCh vesicles beyond those observed for PrP^{WT}-mCh vesicles (Supplementary Movies S1 and S2). Our data indicate that treatment with **CCT020312** at low concentrations can effectively reduce endoggresomes from mammalian axons, and thus can normalize the anterograde and retrograde axonal transport of smaller PrP^{PG14}-mCh vesicles.

Tau aggregates reduced by CCT020312 in a tauopathy frontotemporal dementia disease model

Neurons derived from a frontotemporal dementia (FTD) patient iPSCs, carrying the tau-P301L autosomal dominant mutation, were differentiated for six weeks and treated with CCT020312 for 24 hours at concentrations between 10 nM and 10 μM (Figure 6A). A significant and concentration-dependent reduction in tau was observed (Figure 6B), including of total tau (TAU5 antibody) as well as two phospho-tau (P-tau) epitopes

previously associated with human post-mortem pathology, S396 and S202/T205 (AT8 antibody). Maximum effect was achieved at 10 μM CCT020312 that reduced tau levels to ~20% relative to vehicle control. Importantly, for P-tau S396 a reduction in monomeric tau (~55 kDa band) as well as high MW oligomeric tau (at ≥250 kDa) were both observed.

Based on CCT020312 reduction of total tau and P-tau, compound effect on detergent-insoluble forms of tau, the ones predicted to be more aggregation-prone and toxic, was investigated. Neurons were treated with CCT020312 at the concentrations that caused the strongest reduction in tau (1 μM and 10 μM), and detergent-based protein fractionation of the neuronal lysates was performed as previously described (Guo and Lee, 2011; Kfoury et al., 2012; Silva et al., 2016). By western blot analysis (Figure 6C) and semi-quantitative analysis (Figure 6D), the effect on soluble (S) and insoluble (P) tau fractions was measured. The 1 μM dose had negligible effect on the soluble fraction of tau (Figure 6D, *left*) but reduced insoluble total tau and P-tau by ≥ 50% (Figure 6D, *right*). At the higher dose of 10 μM, CCT020312 reduced soluble tau by ~50%, and significantly reduced insoluble total tau (as detected by the TAU5 antibody) and P-tau S396 by ~100%, with only some detection of P-tau S202/T205 (Figure 6D, *right*). These results indicate a stronger effect by CCT020312 on the insoluble fraction of tau of P301L neurons, particularly at the lower dose.

With the goal of evaluating the longer-term effect of CCT020312 beyond the 24 hours treatment, P301L neurons were treated with 10 μM compound and culture medium was replaced ('washout', Figure 6E *red arrow*). Neurons were collected over a time-course between one and 16 days post-treatment, and total tau and P-tau S396 and S202/T205 levels were measured by western blot (Figure 6E, F). Day zero corresponds to vehicle-treated samples and after 24 hours treatment (day 1), tau was reduced by ~50% (Figure 5F). Notably, after media washout, the levels of total tau and P-tau continued to decrease up to day four, bringing tau levels further down to 0-10% of vehicle-treated samples (Figure 6F). A remarkable prolonged loss of total tau and P-tau was observed up to day 16 post-treatment. In parallel, compound effect on neuronal integrity and neurite outgrowth, by itself or because of tau reduction, was evaluated by measuring

levels of the microtubule protein β-III-tubulin, which remained unchanged during the 16-day period (Figure 6E, F). This suggests that in parallel with CCT020312-mediated tau reduction, neuronal integrity was not affected as per β-III-tubulin and actin levels over time.

CCT020312 treatment decreases tau-P301L neuronal vulnerability to stress

In FTD patient-derived mutant-tau neurons, tau mediated toxicity is represented by increased neuronal vulnerability to stress (Silva *et al.*, 2020). Stressors that reveal this phenotype in tau-P301L neurons include the mitochondrial electron transport chain inhibitor rotenone, high dose of the excitatory neurotransmitter NMDA, and the highly aggregation-prone peptide Aβ(1-42). Treatment with these stressors led to a loss of viability of P301L neurons: 60% loss by 5 μM rotenone (Figure 6G, *top panel*), 60% loss by 400 μM NMDA (Figure 6G, *middle panel*) and >80% loss by 25 μM Aβ(1-42) (Figure 6G, *lower panel*). When neurons were pre-treated with the tau reducing compound CCT020312 for 8 hours and then co-treated with the stressor for an additional 16 hours, there was a consistent protective effect and rescue of neuronal viability (Figure 6G). This was particularly the case for the lower dose of 1 μM CCT020312 that protected neurons from the stressors maintaining viability at ~100%.

Representative immunofluorescence imaging of tau-P301L neurons treated with 1 μM CCT020312 show a clear decrease in P-tau S396/S404 staining relative to vehicle-treated neurons (PHF1 antibody, Figure 6H i-ii) without affecting the MAP2 marker staining or neuronal density/morphology. Neurons treated with CCT020312 also show upregulation and accumulation of autophagy-lysosomal pathway markers, mainly in the cell body, as shown by staining with the lysosomal dye LysoTracker-red (Figure 6H iii-iv), and the lysosomal associated membrane protein LAMP1 (Figure 6H v-vi). These results suggest that tau reduction is a consequence of activation of the autophagy-lysosomal clearance.

Reducing Aβ peptides in Alzheimer's disease direct differentiated neurons

Intrigued by the ability of **CCT020312** treatment to protect tau-P301L neurons from proteotoxic stress mediated by 25 μM Aβ(1-42) treatment, we asked whether **CCT020312** treatment can clear Aβ peptides in AD patient-derived neurons. In previous studies, direct lineage reprogramming has enabled the conversion of adult somatic cells directly into neurons without intermediate pluripotent cells stages.These directly induced neurons (iNs) can substantially preserve age-related changes and recapitulate molecular factors involved in the etiology and pathogenesis of AD. The lack of clearance of Aβ peptides is associated with Aβ aggregation. Increasing evidence indicates that defective lysosomes in neurons promotes intraluminal formation of Aβ fibrils within the compartment as an early-appearing event of extracellular plaque deposits in AD brains. We generated iNs from the fibroblasts of sporadic AD (sAD) and AD carrying A431E mutation in the *PSEN1* gene (AD-PSEN1) donor by an overexpression of pro-neuronal transcription factors (Brn2, Ascl1, Myt1l and Ngn2). The AD-PSEN1 iNs had increased levels of total Aβ and the toxic isoform Aβ(1-42) by ~31% and 38%, respectively, relative to levels in sAD iNs, as measured by immunofluorescence in neuronal cell bodies (Figure 7). We first examined 48-hour treatment of 1 μM BACE-1 inhibitor and found that inhibition of β-Secretase processing lowers the production of total Aβ and Aβ(1-42) in both sAD and AD-PSEN1 iNs by 50-66%. 48-hour treatment of 250 nM rapamycin promoted the reduction of Aβ peptides in both sAD and AD-PSEN1 iNs by ~50%. The result suggests that the activation of autophagy-lysosomal pathway has a beneficial effect on the reduction of Aβ levels in AD patient neurons. Next, we examined whether the **CCT020312** treatment enhances Aβ clearance in neurons. **CCT020312** concentrations below 500 nM were found no detectable cytotoxicity to iNs after 48-hour treatment. Notably, **CCT020312** showed dose-dependent reduction of total Aβ and Aβ(1-42) by ~33-51% in sAD iNs and ~38-50% in AD-PSEN1 iNs. These results suggest that the autophagy-lysosomal activation promotes the removal of Aβ burden in AD patient neurons.

Discussion

We have carried out a high throughput, high content imaging phenotypic screen to identify small molecules that accelerate lipid droplet clearance based on bodipy-based fluorescence imaging. While we have focused our initial efforts on the identification and characterization of hit compounds that hasten LD clearance and exhibit LC3-II-dependent macroautophagy, this screen in fact a “wide net” for discovering small molecules that function through a variety of targets, pathways, and cellular mechanisms, many of which remain to be identified through judicious selection of secondary assays. The use of lipid droplets turned out to be a fortunate choice, as a number of the common macrophagy receptors appear to be used as non-exclusive lipophagy receptors. (Autophagy. 2022 Jul 7;1-4. doi: 10.1080/15548627.2022.2094606. SQSTM1, lipid droplets and current state of their lipophagy affairs Ankit Shroff, Taras Y Nazarko) -

- the levels of LC3-based autophagy flux measured in our assay represents the sum of LC3 needed for all induced autophagy pathways (in many cases presumably more than one). Therefore, compounds with only mild autophagy induction based on our LC3 reporter (0%<X<20% of ratiometric effect observed with Torin-1) and not counted as hits at this point may still induce one specific selective autophagy pathways to greater extent and have a significant impact
- compounds whose activities results in reduction in LDs through LC3-II independent autophagy mechanisms.(LC3 reporter effect close to 0%) – we have identified some compounds that may modulate ERphagy (Stoltz/Dikic lab collaboration). This suggests that changes in the ER membrane-mediated autophagy can modulate LD metabolism independently of LC3-II dependent macroautophagy.
- LC3 dependent non autophagy mechanisms (a couple of recent papers with non-canonical pathway and many more papers with non-canonical autophagy relating to immune cell function, endocytosis.
- Compounds that inhibit lipid biosynthesis/LD biogenesis. – Two DGAT1 inhibitors hits were identified and suggest that we can identify compounds that inhibit LD biosynthesis or biogenesis while allowing continued clearance of LD through lipolysis and lipophagy. It may be feasible to identify tool compounds acting on different steps in the LD biosynthesis and LD biogenesis processes by altering the

timing of oleic acid supplementation or withdrawal and using LD biosynthesis inhibitor for counterscreening (data not shown/unpublished data).

- Lipid efflux activation:Lipophagy-derived fatty acids undergo extracellular efflux via lysosomal exocytosis.Cui W, Sathyanarayan A, Lopresti M, Aghajan M, Chen C, Mashek DG. Autophagy. 2021 Mar;17(3):690-705. doi: 10.1080/15548627.2020.1728097. Epub 2020 Feb 19.
- Autophagy independent functions of autophagy machinery:

Materials and Methods

Cell Culture

SW1990, HEK293T and HeLa cells were purchased from ATCC. HT-1080 cells were purchased from Sigma-Aldrich. U251 cells were a generous gift from The California Institute for Biomedical Research (Calibr). HeLa Difluor (RFP-GFP-LC3) cells were purchased from Invivogen. Cells were cultured at 37 °C and 5% CO 2 in DMEM, RPMI, or MEM supplemented with 10% fetal bovine serum (FBS) and penicillin-streptomycin, as recommended by vendor.

LOPAC pilot screen and High Throughput Screen

SW1990 cells (350 per well) were plated in 8 µL of 10 µM oleic acid supplemented phenol-red free Roswell Park Memorial Institute (RPMI) complete growth media (Gibco) into black-walled clear-bottom 1536-well plates. The oleic acid and bovine serum albumin were purchased from Sigma and the complex was prepared using protocol in (Listenberger and Brown, 2007) or the oleic acid-bovine serum albumin complex was purchased from Sigma. These cells were allowed to grow and adhere for 20 hours. Cells were then treated individually with 4 µM LOPAC library component compounds or individually with 5 µM screening library compounds (940,000 small molecules in total) for 20 hours. Cells were fixed and stained for at least 1 h at room temperature (≈ 25 °C) with a 2 µL addition of a 5X fixative/staining solution (comprising final concentrations of 4% paraformaldehyde, 1 µM BODIPY 493/503, and 0.1 µg/mL Hoechst 33342 fluorophore). Images were collected with a 10X objective on a CellInsight CX5 high content imager employing an LED solid-state light source and filter sets of excitation 485 / emission 521 (BOPIDY 493/503) and ex 386/em 440 (Hoescht) and processed using the Spot Identification algorithm in Cellomics. The entire area of each well was visualized in a single image. Columns of cells were treated with the vehicle control DMSO (final concentration of DMSO in each well was < 0.15 %) and tamoxifen (15 µM) in DMSO

was employed as the positive control. The threshold for primary hit compounds was a > 50 % reduction in total lipid area in comparison to vehicle treated cells, with a ≤ 30 % reduction in cell number. Cell number measurements were determined by counting the nuclei stained with Hoescht in a given image (~230 nuclei were detected in vehicle control wells). All hit compounds were retested in triplicate at 5 μM and the same parameters for advancement were applied (> 50 % reduction in total lipid area, with ≤ 30 % reduction in cell number). Confirmed hits were assessed for dose-dependent activity (10-point dilution ranging from 5 μM to 9 nM). Only compounds demonstrating dose-dependent reduction in cellular lipid load, in addition to a >50% reduction in total lipid area, with ≤30% reduction in cell number at maximum concentration, were progressed. The primary hit rates were 0.65 % for the 940,000 HTS compound collection and 0.98% for the LOPAC constituents.

Counter-screen for fluorescent artifacts and elimination undesirable chemical moieties

The 409 confirmed hits exhibiting dose dependent activity as well as the other attributes described above for progression were subjected to counter-screening. Fluorescent quenching artifacts by the hits were eliminated by counter-screening hit compounds against SW1990 cells fixed before compound administration. All cells possess the same lipid droplet load, so any observed change in lipid droplet fluorescence would be due to a fluorescence quenching interaction of the hit compound with the BODIPY 493/503 fluorophore. SW1990 cells (350 per well) were plated in black-walled clear-bottom 1536-well plates in 10 μM oleic acid supplemented phenol-red free RPMI complete growth media and allowed to adhere for 40-45 h (total incubation period with lipid in primary screen). Cells were fixed via 2 μL addition of a 5X fixative/staining solution (final concentrations of 4% paraformaldehyde, 1 μM BODIPY 493/503, 0.1 μg/mL Hoechst 33342) for 2 hours at room temperature (≈ 25 °C). Cells were then treated individually with primary hit compounds at a concentration of 5 μM for one hour. A column of cells treated with DMSO vehicle (neutral control), while a column of cells was fixed and stained (4% paraformaldehyde, 0.1 μg/mL Hoechst 33342) without a lipid dye (i.e. no BODIPY 493/503) as a positive control. Images were collected with a 10X objective on a CellInsight CX5 high content imager and processed using the same Spot Identification algorithm in Cellomics using Spot Total Area per Cell as previously described. All hits for which the residual activity (BODIPY 493/503 fluorescence decrease in live cells during treatment minus artifactual BODIPY 493/503 fluorescence decrease in fixed cells) was not > 50% were eliminated. In total, 188 compounds were eliminated, leaving 221 compounds. These 221 compounds were manually curated by experienced medicinal chemist (HMP), eliminating pan-assay interference compounds, those bearing significant metabolic liabilities, and compounds that were frequent hits in a wide variety of high-throughput screens, leaving 108 bonafide hits, of which 81 could be reordered as solid stocks.

Confirmation of re-ordered hits

SW1990, U251, and HT-1080 cells (1000 cells / well) were plated in 50 µL of 10 µM oleic acid supplemented RPMI complete growth media (Gibco) into black-walled clear-bottom 384-well plates. The oleic acid and bovine serum albumin were purchased from Sigma and the complex was prepared using protocol in (Listenberger and Brown, 2007) or the oleic acid-bovine serum albumin complex was purchased from Sigma. These cells were allowed to grow and adhere for 20 hours. Cells were then subjected to 10-point dose response curve (10 uM to 0.01 nM) of the aforementioned 81 hits for 20 hours. Cells were fixed and stained via 2 µL addition of a 5X fixative/staining solution (final concentrations of 4% paraformaldehyde, 1 µM BODIPY 493/503, 0.1 µg/mL Hoechst 33342) for at least one hour at room temperature. Plates were washed with DPBS using an automated Biotek automated plate washed. Cell images were collected with a 10X objective on a CellInsight CX5 high content imager, and LED solid-state light source and filter sets of ex 485/em 521 (BOPIDY 493/503) and ex 386/em 440 (Hoescht) and processed using the Spot Identification algorithm in Cellomics using Spot Total Area per Cell. Cellular lipid area was determined relative to lipid load of vehicle-treated cells. Compounds confirmation required a dose-dependent decrease in cellular lipid load as ascertained by a decrease in BODIPY 493/503 fluorescence.

Immunoblot assessment of autophagy

Adherent cells at 75% confluency (150,000 to 300,000 cells) in six-well plates were treated with small-molecules for 20 h. At the conclusion of treatment, the medium and trypsin-aided detached cells were pelleted, washed with PBS, and lysed on ice in RIPA buffer for 30 minutes with intermittent vortexing (50 mM Tris base, 150 mM NaCl, 1% TritonX-100, 0.5% sodium deoxycholate, 0.1% SDS, pH 7.4, with a 1:100 dilution of Halt Protease Inhibitor EDTA-free, 1:100 dilution of Halt Phosphatase Inhibitor, 0.5 µL/mL benzonase). Lysates were clarified (10 minutes at 14,000 rpm, 4°C). Protein content was normalized by BCA Protein Assay reagent (Pierce). Samples were denatured, separated by SDS-PAGE (4−20%), and transferred to a PVDF membrane (Biorad Trans Turbo). Membranes were probed with primary antibodies LC3-I/II (Cell Signaling 2775), phospho S6K (Cell Signaling 9234), S6K (Cell Signaling 2708), and GAPDH (Cell Signaling 2118) overnight at 4°C, then imaged by chemiluminescence with a HRP-conjugated secondary antibody (Cell Signaling 7074).

Human iPSC-derived neurons culture and treatment

Human induced pluripotent stem cell (iPSC)-derived neural progenitor cells (NPCs) corresponding to the WT/WT parental line 7889SA (NYSCF Repository) were acquired from the laboratory of Stuart Lipton. These NPCs were terminally differentiated into cerebrocortical neurons following a standard protocol

(Ghatak et al., 2019). In brief, 300-400,000 NPCs seeded into microscope coverslips were treated with 100nM compound E (EMD Millipore, Temecula, CA) in BrainPhys medium (StemCell Technologies) for 48 hours and then maintained thereafter in BrainPhys medium supplemented with BDNF and GDNF. Upon 7 weeks of differentiation and maturation, quality control histological stainings against NeuN and Ca^{2+} imaging neural activity measurements were done to confirm robust mature neuronal signatures before beginning treatment experiments. The small molecules (250 nM rapamycin, 50 nM CCT020312, 200 nM CCT020312 or vehicle control) were added for 24 hours with DMSO normalized in all conditions to 1% (v/v). For the final 3 hours, cells were also treated with 75 nM LysoTracker Red (Thermo). For the final 30 minutes, Hoechst was added as nuclear stain. A full media change was performed at the 24 hour time point right before imaging in a confocal fluorescence microscope (Nikon C2) at a 10x magnification. 3-5 different fields were randomly selected per coverslip replicate.

TFEB immunofluorescence confocal microscopy

HeLa cells (2.5×10^5) were seeded in 24-well plates containing 12-mm glass coverslips and treated with 0.1% DMSO or 1 μM CCT020312 for 20 h. After treatment, cells were fixed with 4% paraformaldehyde in PBS for 20 min at room temperature, for TFEB staining. Fixed cells were first permeabilized using 0.1% Triton X-100 in PBS for 5 min at room temperature. Then, cells were incubated with a primary antibody against TFEB (CST #4240)(Napolitano et al., 2018) diluted in PBS containing 10% FBS and 0.2% saponin for 2 h at room temperature. Stained cells were then washed three times with PBS and incubated with Alexa Fluor 488-labeled secondary antibodies (Thermo Fisher) diluted at 1:1000 in PBS/10% FBS/0.2% saponin for 1 h at room temperature. Cells were washed three times in PBS, incubated with 4′,6-diamidino-2-phenylindole (DAPI) to label nuclei, and mounted with Prolong® Gold Antifade Reagent. Imaging was performed using a Zeiss ApoTome. For each condition, 15 to 20 images were acquired in randomly selected fields with a 63X oil objective lens. An average of 10 to 15 stacks of 0.3 μm thickness were acquired.

LC3B and LAMP2 immunofluorescence confocal microscopy

HeLa cells (2.0×10^4, 400 μL) were seeded in 8-well Lab-Tek chambered coverglass (Thermo #155409) and treated with 0.1% DMSO, 250 nM rapamycin (Alfa Aesar #J62473), 1 μM CCT020312 or 2.5 μM CCT020312 for 20 h. After treatment, cells were fixed and permeabilized with ice-cold methanol for 10 min in -20°C freezer. Cells were then washed three times with PBS and incubated with a rabbit primary antibody against LC3B (CST #3868) diluted 1:100 in PBS containing 10% FBS and 0.2% saponin overnight at 4°C. Then, LC3B primary antibody was removed and mouse antibody against LAMP2 (Abcam #H4B4) diluted 1:200 in PBS was directly added to the cells for 12 hours at 4°C. After the removal of LAMP2 primary antibody, the cells were washed 3 times with PBS and a mixture of goat anti-

mouse IgG(H+L) cross-absorbed secondary antibody, Alexa Fluor™ 488 (Invitrogen #A-11001) and goat anti-rabbit IgG(H+L) cross-absorbed secondary antibody, Alexa Fluor™ 546 (Invitrogen #A-11035), both diluted 1:500 in PBS, was added to the cells for 2 hours at room temperature. After removal of secondary antibodies, cells were incubated with DAPI (1 µg/mL in PBS) for 5 minutes at room temperature, followed by three washes with PBS. After the washes, 200 µL PBS was added to each well and the chamber slides were subjected to imaging. Zeiss Confocal 780 was used for imaging with 63x oil objective lens, where laser lines 488nm, 561nm and 405nm were used for the excitation of Alexa Fluor™ 488, Alexa Fluor™ 546 and DAPI fluorophores. Images collected were further processed by ImageJ to overlap each channels to give the merged images.

Primary Neuronal Culture

Primary hippocampal neuron cultures were prepared as described previously.(Encalada et al., 2011) Briefly, hippocampi were dissected from 1 to 2-day-old mouse neonates in cold Hank's buffer solution (HBSS) (Gibco) supplemented with 0.08% D-glucose (Sigma), 0.17% HEPES, and 1% Pen-Strep (Gibco), filter sterilized and adjusted to pH 7.3. Dissected hippocampi were washed twice with cold HBSS (Gibco) and individually incubated at 37°C for 15-20 minutes in a sterile solution of 45 U papain (Worthington), 0.01% DNase (Sigma), 1 mg DL-cysteine (Sigma), 1 mg BSA (Sigma) and 25 mg D-Glucose (Sigma) in PBS (Gibco). Hippocampi were washed twice with Dulbecco's Modified Eagle Medium (DMEM) (Gibco) supplemented with 10% fetal bovine serum (FBS) (Gibco) (pre-heated to 37°C) and disrupted by ten to twelve cycles of aspiration through a micropipette tip. Dissociated neurons were then resuspended in warm DMEM (Gibco) + 10% FBS (Gibco) and plated in 24-well plates containing 12-mm glass coverslips pretreated with 50 µg/ml poly-L-lysine (Sigma) in Borate buffer (1.24 g boric acid (Fisher), 1.90 g borax (Sigma), in 500 mL cell-culture grade water, adjusted to pH 8.5, filtered sterilized). After 1 hour, media was replaced with Neurobasal-A medium (NBA) (Gibco), supplemented with 2% B-27 (Gibco) and 0.25% GlutaMAX (Gibco).

Prion Degradation Assay

Hippocampal neurons were transfected at 7 days *in vitro* (DIV) with PrP^{WT}- or PrP^{PG14}-mCherry. 24 hours after transfection, small molecule A5, A15, A18, PI-103 or A18-5 was applied at a final concentration of 50, 200, 500 or 1000 nM and incubated for 2 or 16 hours, after which the media was replaced with fresh Neurobasal-A medium (Gibco) supplemented with 2% B-27 (Gibco) and 0.25% GlutaMAX (Gibco). At 9 DIV, 48 hours post transfection, neurons were fixed. DMSO was used as a control.

Fixation

Neurons were fixed with 4% paraformaldehyde (PFA, Electron Microscopy Services) containing 4% sucrose (Sigma) for 30 min at 37°C. Cells were washed once in 50 mM Glycine in PBS, 3 more times in PBS and once in H_2O before being mounted in ProLong Diamond antifade reagent (Thermo Fisher).

Image Collection and Quantification of Particle Density in Axons

Axons were imaged using a Nikon Ti-E Perfect Focus inverted microscope equipped with a total internal reflection fluorescence (TIRF) setup, with an Andor iXon + DU897 EM Camera, and a 60X/1.49 NA oil objective. A 561 nm laser was used to detect mCherry. Images were taken at 3 field of view away from the cell body.

For PrP^{PG14} aggregate density quantification from still images, we calculated the average axonal background greyvalue. We defined aggregates as those puncta with a grey of at least 2 times the background. Axon length was measured using the polyline tool of ImageJ. Aggregate density was expressed as the average number of aggregates per 100 µm of axon length.

ARE-LUC Reporter Assay

IMR32 cells were plated at 5000 cells per well in white, clear bottom 384-well plates in 40 µL growth medium. The next day, 100 ng pTI-ARE-LUC reporter plasmid in 10 µL OptiMEM (Gibco) was transected into each well using Fugene HD at a dilution of 1 µg plasmid DNA:4 µL Fugene. After 24 hours, compounds were transferred using a 100 nL pintool head affixed to PerkinElmer FX instrument. After 24 hours of compound incubation, ARE-LUC luminescence values were recorded on an Envision instrument (PerkinElmer) after the addition of 30 µL BrightGlo reagent solution (Promega), diluted 1:3 in water.

Dynamic light scattering measurements

Liposomes for the DLS were prepared by dispersing 10 mg/mL of dipalmitoylphosphatidylcholine (DOPC) in chloroform (Avanti) in a test tube and drying under argon to afford a thin lipid film. The lipid film was hydrated with deionized water and extruded 31 times through a 200 nm filter at room temperature, which was subsequently diluted and placed in a disposable cuvette for DLS analysis. **CCT020312** was dissolved in deionized water or DPBS (Gibco) at a concentration of 1 µM, 10 µM, or 50 µM. The solution was then centrifuged at 9000 x g for 10 min. The resulting solution was transferred to a plastic cuvette for DLS analysis. Size distribution as measured on the DLS measurements was carried out at 20 °C. 20 measurements were done with a data acquisition time of 10 s each.

Lipid quantification by mass spectrometry

For MS analysis of lipids, whole cell pellets were resuspended in 1 mL of a cold hypotonic buffer consisting of 1 mM PBS, pH 7.4. The material was then homogenized on ice using a glass Dounce homogenizer (30 strokes). The homogenized sample was transferred to a pre-weighed 1.5-mL microfuge tube and lyophilized overnight. The lyophilized material and tube was weighed and normalized by total mass prior to performing a modified Bligh and Dyer extraction.(Bligh and Dyer, 1959). The proceeding steps were done with glass pipettes and tubes to avoid plastic contamination. Total lipids were extracted by the addition of 1 mL Milli-Q H_2O containing 5 mM erythorbate with 2 mL of cold methanol (CH_3OH) containing lipid class standards (Splash Lipidomix 330707, Avanti) at a dilution of (1:50), followed by the addition of 2 mL of cold chloroform ($CHCl_3$) with occasional vortex mixing and shaking. The sample was agitated and centrifuged in glass test tubes at 100 x g for 5 min. The bottom organic phase was collected in a clean test tube, while the upper phase was re-extracted three additional times with the first containing 1 mL CH_3OH:$CHCl_3$ (1:1, v/v), second with 1 mL $CHCl_3$ and the third with 1 mL $CHCl_3$ containing HCl at final concentration of 10 mM. The organic phases were combined and dried under vacuum to afford a lipid film that was stored at −80°C until MS analysis.

Extracted lipid samples stored under argon were removed from the −80° C freezer and were resuspended in 200 µL of methanol. Positive and Negative mode LC-MS analysis was performed on an Agilent 6230 ESI-TOF-MS System calibrated with a reference solution at m/z 1033.9881. A XBridge BEH C8 XP Column (Waters, 2.5 µm, 4.6 mm X 150 mm) was used at a flow rate of 500 µL/min, employing the following gradient: 30 to 100% solvent B over 30 min, 100% isocratic B for 10 min followed by a return to 30% B for 5 min. Solvents A consisted of MilliQ water and methanol (9:1, v:v). Solvents B consisted of acetonitrile: 2-propanol (5:3, v:v), and both contained 10 mM Piperidine, 10 mM ammonium acetate (or 10 mM sodium acetate) and 0.1% formic acid. Prior to processing, raw.d files were converted to the open format mzXML using MSConvert software, which is part of the ProteoWizard software toolkit.(Chambers et al., 2012) Mass detection was achieved using mzmine 2 wavelet algorithm, ADAP chromatogram builder and ADAP deconvolution95, which are part of the MZmine 2 software package.(Pluskal et al., 2010) Initial lipid identifications were achieved using lipidmaps database with a m/z tolerance of 15 ppm, subsequently detected lipids were filtered out for further processing. The putative lipid peaks were validated by aligning to the internal standards. The quantification of all lipid classes was normalized based on the abundance of the internal standard corresponding to that class, which factors in extraction efficiency and sample handling.

Human FTD Neural Progenitor Cell Lines

Work with human induced pluripotent stem cells (iPSC) and the derived neural progenitor cell (NPC) lines was executed under the Massachusetts General Hospital/Mass General Brigham-approved IRB Protocol

#2010P001611/MGH. Patient-specific iPSCs and cortical-enriched NPCs were generated as previously described.(Seo et al., 2017; Silva *et al.*, 2016) In this study, the NPC line used is designated MGH2046-RC1 and is derived from an individual in her 50s with FTD and carrier of the tau-P301L autosomal dominant mutation (c.C1907T, rs63751273).(Seo *et al.*, 2017; Silva *et al.*, 2016)

NPC Culture, Differentiation and Compound Treatment

NPCs were cultured in 6-well (Fisher Scientific Corning) or black 96-well clear bottom (Fisher Scientific Corning) plates coated with poly-ornithine (20 µg/mL in water, Sigma) and laminin (5 µg/mL in PBS, Sigma), referenced to as POL-coated plates. NPC proliferation medium composition was as follows: 70% (v/v) DMEM (Gibco), 30% Ham's-F12 (v/v) (Fisher Scientific Corning), 2% B27 (v/v) (Gibco), and 1% penicillin-streptomycin (v/v) (Gibco); freshly supplemented with 20 ng/mL EGF (Sigma), 20 ng/mL FGF (Stemgent) and 5 µg/mL heparin (Sigma) at the time of cell passaging, which was done using TrypLE reagent (Thermo Fisher). For neural differentiation over the course of six to eight weeks, cells were plated at an average density of 80,000 cells/cm^2 in 6-well (in 2 mL medium volume) or 96-well (in 200 µL medium volume) plates POL-coated, in the same NPC media but without growth factors. Neuronal cultures feeding consisted of half medium volume changes twice a week.(Silva *et al.*, 2016) Compound treatment in 6-well plate format was performed by removing 1 mL of medium from the culture and adding 1 mL of new medium pre-mixed with the compound at the appropriate 2X final concentration (final volume 2 mL), followed by incubation at 37°C for the designated time. For compound treatment in 96-well plates, cells were in 100 µL and compound was added directly to the medium at 1X final concentration. CCT020312 synthesized in the Kelly lab (JX) was used. As a control, neurons were treated with vehicle alone (DMSO 0.1% (v/v)) which corresponds to the 0 µM CCT020312 concentration.

Neuronal Cell Lysis and Western Blot Analysis

Neurons differentiated and treated in 6-well plates were washed with DPBS (Corning), detached from the well into suspension by scrapping, transferred to Eppendorf tubes, and centrifuged at 3,000 *x g* for 5 min. Cell pellets were lysed directly in 8X the cell pellet volume with 2% SDS blue loading buffer (New England Biolabs), containing DTT, incubated at room temperature for 15 min, and boiled for 15 min prior to SDS-PAGE. Electrophoresis was performed with 10 µL of sample per well using the Novex NuPAGE SDS-PAGE Gel System (Invitrogen). Proteins were transferred from the gel onto PVDF membranes (EMD Millipore) using standard methods. Membranes were blocked in 5% (w/v) BSA (Sigma) in Tris-buffered saline with Tween-20 (TBST, Boston Bio-Products), and incubated overnight in primary antibody prepared in 5% (w/v) BSA-TBST at 4°C. After membrane washing in TBST, these were incubated with the corresponding HRP-linked secondary antibody at 1:4000 dilution (Cell Signaling Technology). Membranes

were incubated with SuperSignal West Pico Chemiluminescent Substrate (ThermoFisher) according to manufacturer's instructions and exposed to autoradiographic films (LabScientific by ThermoFisher). Imaging capture was done with an Epson Perfection V800 Photo Scanner. Protein bands' densitometry quantification (pixel mean intensity in arbitrary units, a.u. or OD) was done with Adobe Photoshop 2021 Histogram function and normalized to the respective internal control (β-Actin or GAPDH) band. Calculations were performed in Microsoft Excel (v.16.59), and graphs were plotted in GraphPad Prism 9. The antibodies used were as follows: total tau TAU5 from Invitrogen (AHB0042), P-tau Ser202/Thr205 or AT8 from Thermo Scientific (MN1020), P-tau Ser396 from Invitrogen (44752G), β-III-tubulin from Sigma (T-8660), GAPDH from Abcam (ab8245), and β-ACTIN from Sigma (A1978).

Protein Solubility Analysis

Cell lysis and fractionation based on protein differential solubility to detergents Triton-X100 and SDS was performed as previously described. (Guo and Lee, 2011; Kfoury *et al.*, 2012; Silva *et al.*, 2016) Briefly, cell pellets corresponding to two wells of a 6-well plate (double-well pellet with same treatment conditions) were lysed in 1% (v/v) Triton-X100 buffer (Fisher Scientific) in DPBS supplemented with 1% (v/v) Halt Protease/Phosphatase inhibitors (Thermo Fisher Scientific), 1:5000 Benzonase (Sigma) and 10 mM DTT (New England BioLabs). Lysates were centrifuged at 14,000 *x g* for 10 min at 4°C and the supernatants containing higher solubility proteins (S fractions) were transferred to new tubes. The pellets were resuspended in 5% (v/v) SDS (Sigma) RIPA buffer supplemented with 1% (v/v) Halt Protease/Phosphatase inhibitors (Thermo Fisher Scientific), 1:5000 Benzonase (Sigma) and 10 mM DTT (New England BioLabs), and centrifuged at 20,000 *x g* for 2 min at 20°C. The new supernatants contain protein of lower solubility/insoluble (P fractions). SDS-PAGE western blot was performed by loading 20 µg of each S-fraction and equal volume of the P-fraction onto pre-cast Tris-Acetate SDS-PAGE (Novex, Invitrogen). Western blots were performed as before. Densitometry quantification (pixel mean intensity in arbitrary units, a.u. or OD) was done with the Histogram function of Adobe Photoshop 2021 and normalized to the respective GAPDH intensity in the S-fraction. Calculations were done in Microsoft Excel (v.16.59) and graphs were plotted in GraphPad Prism 9.

Time-Course Analysis of Tau Levels

Neurons were differentiated for six weeks and on day 0, vehicle alone (DMSO) or compound **CCT020312** was added to the neuronal cultures and incubated for 24 hrs at 37 °C. On day 1, neuronal medium was replaced with new medium without compound (compound washout). At each time point after the 24 hrs treatment and up to 16 days post-treatment, one well of cells was sacrificed for direct lysis in 2% SDS blue

loading buffer (New England Biolabs) and protein analysis of tau and β-III-tubulin (Sigma T-8660) by western blot as described above.

Stress vulnerability assays

Performed as previously described.(Silva *et al.*, 2016) Briefly, NPCs were plated at an average density of 90,000 cells/cm^2 in 96-well plates (black, clear flat bottom, Corning), and differentiated for eight weeks. Compound **CCT020312** (1 μM or 10 μM) or DMSO (Sigma) were added directly onto the media and incubated for 8 hrs at 37 °C. Then, wells were treated with either 25 μM Aβ(1-42) (Abcam), 400 μM NMDA (Enzo LifeSciences), 5 μM rotenone (Sigma), or vehicle/DMSO alone, for an additional 16 hrs. At 24 hrs, viability was measured as described above, with alamarBlue HS cell viability reagent (Thermo Fisher) at 1:10 dilution with 3 hrs incubation at 37 °C, according to manufacturer's instructions. Calculations and statistics were done in Microsoft Excel version 16.59; graphs were plotted in GraphPad Prism 9.

Immunofluorescence of neuronal cells

NPCs were plated at a starting density of 90,000 cells/cm^2 in black POL-coated 96-well clear-bottom plates (Corning), in DMEM/F12-B27 media and differentiated for six weeks, followed by compound treatment for 24 hrs. For LysoTracker live cell staining, cells were incubated with LysoTracker Red DND-99 (Life Technologies L-7528) at 500 nM for 45 min at 37 °C, according to manufacturer's protocols. Then, all neurons were fixed with 4% (v/v) formaldehyde-PBS (Tousimis) for 30 min, washed in DPBS (Corning), and incubated for 2 hrs with permeabilization/blocking buffer with the following composition: 10 mg/mL BSA (Sigma), 0.05% (v/v) Tween-20 (Bio-Rad), 2% (v/v) goat serum (Life Technologies), 0.1% Triton X-100 (Bio-Rad), in PBS. Cells were then incubated with primary antibodies overnight at 4 °C: P-Tau PHF1 (kind gift from Dr. Peter Davies), MAP2 (Millipore AB5543), LAMP1 (Cell Signaling Technology 9091) and Hoechst 33342 (Thermo Fisher). Afterwards, cells were washed with PBS and incubated with the corresponding AlexaFluor-conjugated secondary antibodies (Life Technologies). Image acquisition was done with the InCell Analyzer 6000 Cell Imaging System (GE Healthcare Life Sciences) and micrographs were assembled using Adobe Photoshop 2022.

Statistical Information

Graphed data represent mean values and error bars represent SD (standard deviation) or SEM (standard error of the mean), calculated using Microsoft Excel and GraphPad Prism. P-value < 0.05 was considered the threshold for statistical significance. P-value significance intervals (*) are provided within each figure legend, together with the statistical test performed for each experiment. N values are indicated within figure legends and refer to biological replicates (NPC differentiation cultures independent setup and analysis, at

different times), whereas technical replicates refer to the repeated analysis of the same samples. Derived statistics correspond to analysis of averaged values across biological replicates.

Human dermal fibroblast cell culture and direct neuronal differentiation

Human dermal fibroblasts were acquired from Stanford Alzheimer's Disease Research Center (ADRC). Cells were cultured in DMEM medium with high glucose and GlutaMAX containing 10% Fetal Bovine Serum, 1% Penicillin-Streptomycin, MEM Non-Essential Amino Acids, 1% sodium pyruvate and 0.1% beta-mercaptoethanol (ThermoFisher Scientific).

To generate directly induced neurons (iNs), fibroblasts were transduced with lentiviral vectors of FUW-M2rtTA and doxycycline-inducible Ngn2-puro, Ascl1, Brn2 and Myt1l. The transduced cells were selected by 0.5 µg/mL puromycin (ThermoFisher Scientific) for 2 days and then received magnetic cell sorting to enrich the PSA-NCAM-positive cells. These PSA-NCAM-positive cells were replated onto the poly-L-ornithine/laminin coating coverslips and cultured in the Reprogramming Medium: DMEM/F-12 and neurobasal medium supplemented with 0.25% GlutaMAX, 1% N-2, 2% B-27 and 1% Penicillin-Streptomycin (ThermoFisher Scientific) for 3 weeks. The Reprogramming Medium was added with 5 µM Forskolin (Sigma-Aldrich), 2 µM Dorsomorphin (Tocris), 10 µM SB-431542 (Tocris), 1 µg/mL doxycycline (Cayman), 10 ng/mL BDNF (Peprotech) and 10 ng/mL NT-3 (Peprotech) to promote neuronal differentiation. Then, the cells were switched to Neuronal Medium: BrainPhys neuronal medium (STEMCELL Technologies) supplemented with 0.25% GlutaMAX, 1% N-2, 2% B-27, 1% Penicillin-Streptomycin (ThermoFisher Scientific) and 5 µM Forskolin (Sigma-Aldrich), 2 µM Dorsomorphin (Tocris), 10 µM SB-431542 (Tocris), 1 µg/mL doxycycline (Cayman), 10 ng/mL BDNF (Peprotech) and 10 ng/mL NT-3 (Peprotech) to promote neuronal maturation, and cultured for additional 2 weeks. Half of the culture medium was changed every 2-3 days.

iNS immunofluorescence

iNS were plated at a starting density of XXX in XXX plates/slides, in XXX media and treated with 0.1% DMSO, 1 µM β-Secretase Inhibitor IV (Sigma #565788) for 48 hours. Then, all neurons were fixed with XX for XX min, washed in DPBS, and incubated for XX hrs with permeabilization/blocking buffer. Cells were then incubated with primary antibodies at XX dilution overnight at 4 °C: Amyloid β (D54D2) (Cell Signaling), Amyloid β A4 (CT, 1-42) (8G7) (Enzo Life Sciences). Afterwards, cells were washed with PBS and incubated with XX secondary antibodies at XX dilution for XX hours at room temperature. Image acquisition was done with the XX microscope. Images were analyzed by calculating mean fluorescence

intensity of total Aβ and Aβ(1-42) in the cell body of individual neuron. The total cell number used for data analysis in each condition is ranging from 88 to 142 from three independent experiments.

Synthesis of CCT020312

CCT020312 was synthetized using a modified method following literature procedure.[i]

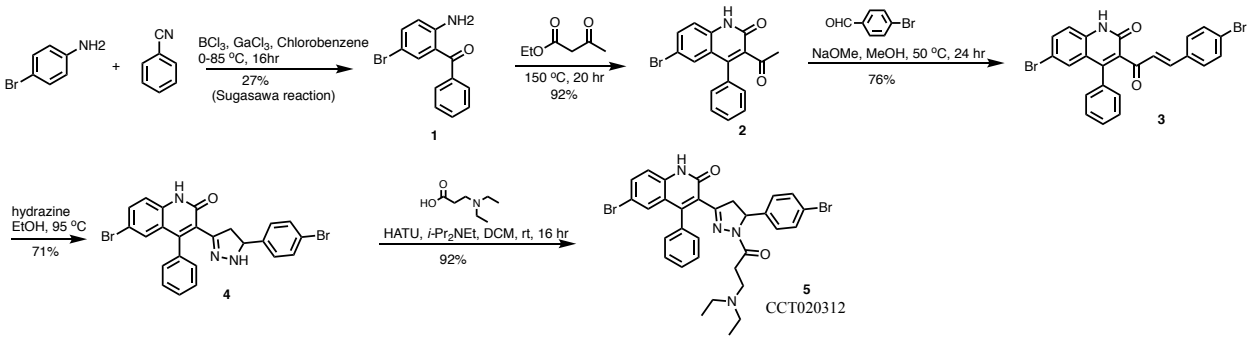

Supplemental Scheme 1. Synthesis of CCT020312 (**5**)

(2-Amino-5-bromophenyl)(phenyl)methanone (**1**)

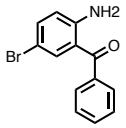

To the stirred solution of 4-bromoaniline (10.32 g, 60.00 mmol) in anhydrous chlorobenzene (200 mL) was added boron trichloride (1M in heptane, 90 mL, 90.00 mmol, 1.5 equiv.) slowly at 0 °C under an argon atmosphere. After about 5 min, benzonitrile (12.35 g, 120.00 mmol, 2.0 equiv.) and gallium chloride (12.68g, 72.00 mmol, 1.2 equiv., dissolved in 50 mL of chlorobenzene) were added slowly via syringe. The reaction mixture was raised to room temperature and stirred for 1 h, then raised to 85 °C and stirred for another16 h, and cooled to room temperature. HCl (4N, 100 mL) was added and the mixture was again raised to 100 °C and stirred for 30 min. The mixture was cooled to room temperature and diluted with water (100 mL). The organic phase was extracted with EtOAc (3x100 mL), washed with brine, dried over Na_2SO_4 and concentrated under reduced pressure. The crude product was purified by CombiFlash silica gel column chromatography using gradient elution with 0-20% EtOAc in hexane to afford compound **1** (4.52g, 27.4%) as a yellowish powder.
^{1}H NMR (600 MHz, Chloroform-*d*) δ 7.63 (d, *J* = 7.7 Hz, 2H), 7.58-7.54 (m, 2H), 7.52-7.46 (m, 2H), 7.37 (dd, *J* = 8.8, 2.8 Hz, 1H), 6.67 (d, *J* = 8.8 Hz, 1H). ESI-MS (m/z): 276/278 $[M+H]^+$.

3-Acetyl-6-bromo-4-phenylquinolin-2(1*H*)-one (**2**)

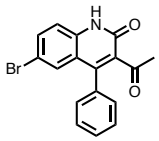

The mixture of compound **1** (4.40 g, 15.94 mmol) and ethyl acetoacetate (15 mL, excess amount) was stirred at 150 °C for 20 h, then cooled to room temperature. The precipitate was filtered and washed with cold diethyl ether (3x10 mL), dried under vacuo to afford pure product **2** (5.04 g, 92%) as white powder. ^{1}H NMR (400 MHz, Methanol-d_4) δ 7.70 (dd, *J* = 8.8, 2.2 Hz, 1H), 7.57-7.52 (m, 3H), 7.37-7.32 (m, 3H), 7.27 (d, *J* = 2.2 Hz, 1H), 2.21 (s, 3H). ESI-MS (m/z): 342/343 $[M+H]^+$.

(*E*)-6-Bromo-3-(3-(4-bromophenyl)acryloyl)-4-phenylquinolin-2(1*H*)-one (**3**)

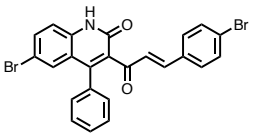

To the solution of **2** (1198 mg, 3.50 mmol) and 4-bromobenzaldehyde (777 mg, 4.20 mmol, 1.2 equiv.) in methanol (60 mL) was added sodium methoxide (416 mg, 7.70 mmol, 2.2 equiv.) at room temperature. The mixture was raised to 50 °C and stirred for 24 h then cooled. The reaction was then quenched and neutralized by addition of 4N HCl slowly, diluted with water (~50 mL). The solution was evaporated under reduced pressure to remove most of methanol. The organic phase was then extracted with EtOAc (3x100mL), washed with brine, dried over Na_2SO_4 and concentrated under reduced pressure. The crude product was purified by CombiFlash silica gel column chromatography using gradient elution with 0-50% EtOAc in hexane to afford compound **3** (1624 mg, 76%) as a pale-yellow solid.
^{1}H NMR (500 MHz, Chloroform-*d*) δ 7.57 (dd, *J* = 8.8, 1.8 Hz, 1H), 7.44 (d, *J* = 8.4 Hz, 2H), 7.42-7.36 (m, 4H), 7.29 (d, *J* = 8.8 Hz, 1H), 7.28-7.21 (m, 5H), 6.65 (d, *J* = 16.2 Hz, 1H). ESI-MS (m/z): 508/510/512 $[M+H]^+$.

6-Bromo-3-(5-(4-bromophenyl)-4,5-dihydro-1*H*-pyrazol-3-yl)-4-phenylquinolin-2(1*H*)-one (**4**)

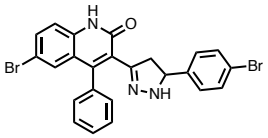

The mixed solution of **3** (1624 mg, 3.19 mmol) and hydrazine hydrate (50-60%, 817 mg, 794 uL, *ca* 12.8 mmol) in EtOH (100 mL) was stirred at 95°C for 20 h and cooled. The yellow precipitate was filtered, washed with EtOH, and vacuum dried. The filtrate was concentrated, then partitioned between dichloromethane and water. The organic phase was washed with brine, dried over Na_2SO_4, and concentrated under reduced pressure to give a yellow solid, which was combined with above treated yellow precipitate to afford product **4** (1180 mg, 71% yield).
^{1}H NMR (500 MHz, Chloroform-*d*) δ 7.54 (dd, *J* = 8.6, 2.1 Hz, 1H), 7.53-7.41 (m, 2H), 7.37-7.16 (m, 7H), 6.94 (d, *J* = 8.3 Hz, 2H), 4.67 (t, *J* = 10.8, 7.5 Hz, 1H), 3.23-3.11 (m, 1H, hidden), 2.63 (dd, *J* = 17.1, 7.5 Hz, 1H). ESI-MS (m/z): 522/524/526 $[M+H]^+$.

CCT020312: 6-Bromo-3-(5-(4-bromophenyl)-1-(3-(diethylamino)propanoyl)-4,5-dihydro-1*H*-pyrazol-3-yl)-4-phenylquinolin-2(1*H*)-one (**5**)

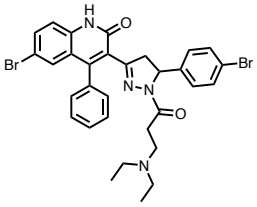

To the solution of **4** (523 mg, 1.00 mmol), 3-(diethylamino)propionic acid (273 mg, 1.88 mmol) and diisopropylethylamine (348 uL, 2.00 mmol) in anhydrous DMF (10 mL) was added 1-[bis(dimethylamino)methylene]-1*H*-1,2,3-triazolo[4,5-b]pyridinium 3-oxide hexafluorophosphate (or HATU) (684 mg, 1.80 mmol) at room temperature. The mixture was stirred at room temperature for 16 h. The solvent was removed under reduced pressure and the crude product was purified firstly by CombiFlash silica gel column chromatography using gradient elution with 0-15% MeOH in DCM to followed by further purification by preparative HPLC to afford compound **5** (600 mg, 92%) as a pale-yellow to white solid.
Preparative HPLC condition: Agilent preparative HPLC system; Column: Phenomenex Gemini-NX C18, 30x250 mm; Mobile phase: 10% (1min) – 10% to 95% (20 min) – 90% (5min) of MeCN in water with 0.1% TFA; Flow rate: 30 mL/min; t_R = 14.6 min.

DMSO

^{1}H NMR (600 MHz, Chloroform-*d*) δ 11.93 (s, 1H), 7.63 (dd, *J* = 8.7, 2.1 Hz, 1H), 7.62-7.59 (m, 1H), 7.56-7.52 (m, 2H), 7.40-7.35 (m, 3H), 7.29 (d, *J* = 8.7 Hz, 1H), 7.27 (d, *J* = 2.2 Hz, 1H), 7.23-7.20 (m, 1H), 6.78 (d, *J* = 8.4 Hz, 2H), 5.29 (dd, *J* = 11.9, 4.3 Hz, 1H), 3.74 (dd, *J* = 18.4, 11.9 Hz, 1H), 3.35-3.24 (m, 2H), 3.18-2.88 (m, 7H), 1.30 (t, *J* = 7.3 Hz, 3H), 1.25 (t, *J* = 7.3 Hz, 3H). ^{13}C NMR (151 MHz, Chloroform-*d*) δ 166.3, 161.4, 152.9, 151.9, 139.6, 136.3, 134.4, 133.9, 131.5 (2C), 130.0, 129.3, 128.5, 128.4, 128.2, 128.1, 127.2 (2C), 122.9, 121.5, 121.3, 117.2, 115.8, 59.0, 46.3, 46.2, 46.0, 44.9, 28.4, 7.91, 7.89. HRMS (ESI-TOF) m/z: calcd for $C_{31}H_{31}Br_2N_4O_2^+$: 649.0808, 651.0788, 653.0767; found for $[M+H]^+$ 649.0838, 651.0824, 653.0808.

Assessment of drug purity by analytical HPLC

Supplemental Figure XX. Analytical HPLC spectra of CCT020312 (**5**):
Agilent Technologies, 1260 infinity. Waters Symmetry C18, 4.6x75 mm, MeCN in water with gradient 20% MeCN (1min)-20%-95% (9min)-95%(5min), flow rate at 1mL/min.

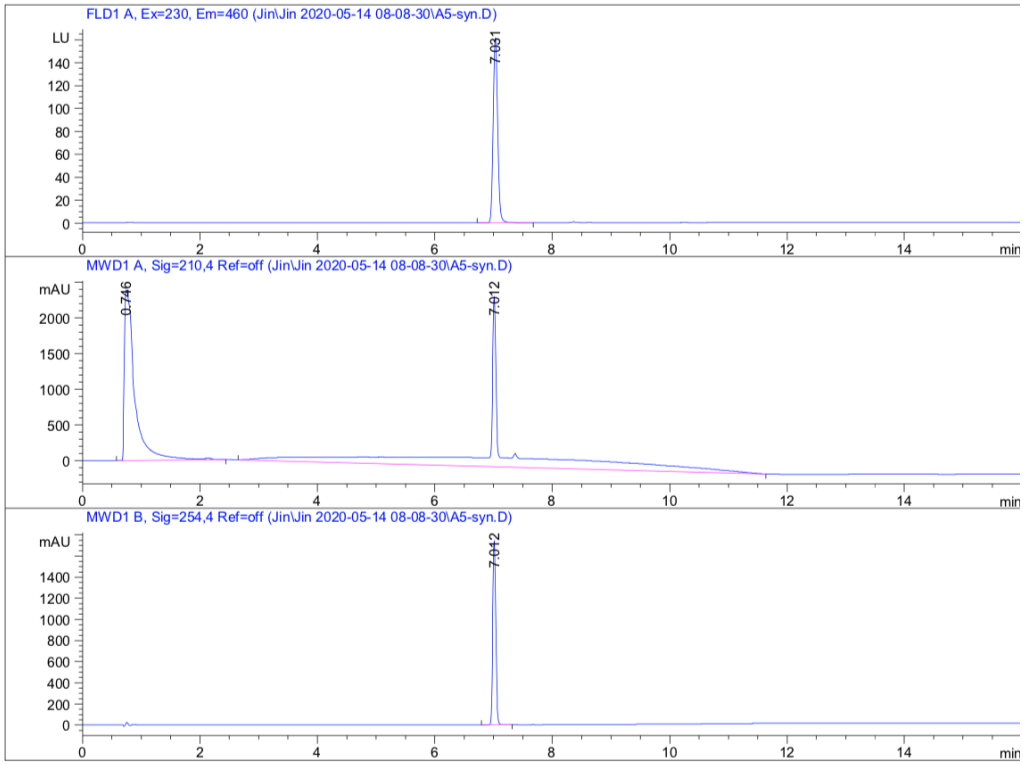

Supplemental Figure XX. Analytical HPLC spectra of carboxy-CCT020312:

2.7. Mass Spectrometry-Based Quantitative Proteomics Experiments

After 24 h of transgene expression, HEK293T cells were lysed with 1 × RIPA buffer and subjected to TMT labeling and mass spectrometry as previously described [20]. In brief, the protein was precipitated in chloroform and methanol, then dissolved in Rapigest (Waters, Milford, MA, USA). Disulfide bonds were reduced using TCEP (tris(2-carboxyethyl)phosphine) (Thermo Fisher, Waltham, MA, USA) in HEPES (4-(2-hydroxyethyl)-1-piperazineethanesulfonic acid) (Thermo Fisher)-buffered solution, followed by S-alkylation with chloroacetamide (Thermo Scientific). Samples were then enzymatically digested with Porcine Trypsin (Promega, Madison, WI, USA) overnight and then labeled using 11-plex Tandem Mass Tags (TMT) Isobaric Mass Tag labeling reagents (Thermo Fisher). TMT labeled samples were then combined and fractionated using the Pierce High pH Reversed-Phase Peptide Fractionation Kit (Thermo Scientific). Fractionated samples were then injected onto a C18 analytical column and subjected to MS1 and MS2 fragmentation on a Thermo Scientific Q Exactive HF Orbitrap. Protein identification and quantification were performed using the Integrated Proteomics Pipeline (IP2) [21,22]. Tandem mass spectra in the form of MS1 and MS2 files were searched against the current reviewed UniProt human protein database.

Figure Legends.

Figure 1: *Lipid droplet degradation screen identifies novel autophagy activators.* (**A**) Schematic representation of macroautophagy. Cytosolic cargo is sequestered in an LC3-dependent manner into *de novo*-synthesized, double-membrane-bound autophagosomess that subsequently fuse with lysosomes to degrade their contents. (**B**) Schematic representation of the process to set-up and optimize a cell-based, high-throughput screen for the identification of small molecules (compounds) accelerating lipid droplet clearance. Parameters chosen for the final screen setting are indicated in bold. The screen uses a fluorescent probe, BODIPY 493/503, that accumulates in hydrophobic environments like lipid droplets. Cells treated with vehicle control display higher number and area of fluorescent punctae relative to cells treated with autophagy activator compounds. (**C**) Schematic representation of the screening pipeline employed to identify and prioritize compounds that clear lipid droplets out of a 1 million compound library. The number of hits remaining at each step of the validation process is indicated in bold. The pipeline includes a primary screen to identify compounds that clear lipid droplets dose-dependently in a non-cytotoxic manner, the removal of compounds that are known fluorescent artifacts, quenchers, or PAINS, the validation of lipid droplet clearance in multiple immortalized cell lines, and a final autophagy flux screen. (**D**) Heatmap of normalized lipid droplet clearance data in SW1990 cells fed with 10 µM oleic acid followed by treatment with 77 hit compounds at different concentrations (1.3 nM ≤ C ≤ 25 µM). The heat map tiles of compound 35 (**CCT020312**) are surrounded with a black outline. (**E,F**) Autophagy flux screen of 120 compounds in RPE1 cells using the reporter GFP-LC3-RFP-LC3ΔG. (**E**) Heatmap representing the difference between the average (n = 3) of GFP/RFP ratio of total integrated fluorescence intensities of individual compounds at three different concentrations (0.05, 0.5 and 5 µM) to the average (n = 18) GFP/RFP ratio of DMSO. (**F**) Heatmap representing the difference between the slope of individual compounds and DMSO (n = 3): the slope of each subsequent set of two timepoints was averaged and compared to respective DMSO data. Red represents higher autophagy flux and green lower autophagy flux induction than DMSO. Threshold of heatmaps were adjusted to fully represent the whole set of data. Blue and orange arrows refer to Supplementary Figure 1J.

Figure 2: *CCT020312 induces autophagic flux*. (**A**) Chemical structures of CCT020312, inactive analog carboxy-CCT, and active analog ANP990/C48. (**B**) Representative images of SW1990 cells fed with 10 µM oleic acid followed by 20h treatment with 0.1% DMSO or 2.7 µM CCT020312. Lipid droplets and nuclei are stained with BODIPY 493/503 fluorescence (green) and Hoechst 33342, respectively. **C**) CCT020312 dose response curve from SW1990 cells fed with 10 µM oleic acid followed by 18h treatment. Points and error bars depict mean ± s.e.m. ** Holm multiple comparison test following one-way ANOVA $p < .01$, **** $p < .0001$. (**D**) Percent of autophagy flux over time in RPE1 cells stably expressing the reporter GFP-LC3-mCherry-LC3ΔG and treated with different concentrations of CCT020312. For details see also Supplemental Fig.1I. (**E**) Growth curves corresponding to (**D**). (**F**) Plot depicting difference between the green/red ratio of total integrated fluorescence intensities reflecting the difference in autophagy flux of CCT020312 and carboxy-CCT (inactive analog) over time. Higher numbers represent higher autophagy flux upon CCT020312 treatment in comparison to carboxy-CCT treatment at the same concentration. Statistical significance for each time point has been calculated by one-sided Student's T-distribution and indicated as a circle; n = 8; empty circle: not significant ($p \geq 0.05$; increasing size of filled circle is proportional to the increasing significance of the data point. (**G**) Example Western blot analysis of HeLa cells treated with indicated

concentrations of compounds over 4.5 h (upper panel) as well as corresponding LC3B quantification (lower panel; n = 3). BafA1 = 0.2 µg/mL Bafilomycin A1. (**H**) Optical pulse labeling enables tracking of protein degradation. Upper panel: representation of a LC3B degradation assay with photoconvertible Dendra2 linked to LC3B over time. Lower panel: Half-life of Dendra2-LC3 transfected in primary mouse cortical neurons upon treatment of indicated compounds. DMSO serves as control. Bars and error bars depict mean + s.e.m., n = 116. * Dunnett's multiple comparison test following one-way ANOVA $p < .05$, ** $p < .01$, *** $p < .001$, **** $p < .0001$. (**I**) Quantification of the normalized DALGreen fluorescence area and DALGreen/DAPRed fluorescence area ratio in human iPSC-derived cerebrocortical neurons after 24 hour treatment with CCT020312 or DMSO. **** Dunn's multiple comparison test following Kruskal-Wallis $p < .0001$. (**J**) Representative images of human iPSC-derived cerebrocortical neurons stained with DALGreen and DAPRed after 24 hour treatment with 50 nM or 200 nM CCT020312 or DMSO.

Figure 3: CCT020312 activates autophagy independent of mTORC1. (**A**) Bar graph representing the percentage of HeLa cells eliciting TFEB nuclear localization calculated from fluorescence microscopy images (representative images shown) taken after 20 hours of treatment with DMSO (vehicle) or 1 µM CCT020312 (total ~1,800 cells, $N = 53$ images per condition, from three independent experiments). Unpaired t-test **** $p < .0001$. (**B**-**E**) HeLa cells treated with 250 nM Torin-1, 1 µM CCT020312 or DMSO for 20 hours and immunoblotted for (**B**) phospho-TFEB (S211), (**C**) phospho-S6K (T389), (**D**) phospho-4EBP1 (T37, T46) and (**E**) phospho-ULK1 (S757). Bar graph depicts quantification of n = 3 replicates, one representative Western blot shown. (For (D), DMSO and Torin-1 bar graph depicts quantification of n = 5 replicates.) * Dunnett's multiple comparison test following one-way ANOVA $p < .05$, ** $p < .01$, *** $p < .001$. (F-H) U251 cells treated with 250 nM Torin-1, CCT020312 (10 nM, 100 nM or 1 µM) or DMSO for 20 hours and immunoblotted for (**F**) phospho-S6K (T389), (**G**) phospho-4EBP1 (S65) and (H) phospho-ULK1 (S757).

Figure 4: (**A**) Volcano plot depicting RNA-Seq analysis of HEK293T cells treated with 1 µM CCT020312 for 20 hours. (**B**) Gene set enrichment analysis of adjacent RNA-Seq data for activation of stress-responsive signaling pathways: PERK, ATF6 and IRE1/XBP1s arms of the unfolded protein response, heat shock response (HSR), oxidative stress response (OSR) and other genes. (**C**) Lipidomics time course of HEK293T cells performed during autophagy activation. HEK293T cells were treated for 2, 12 or 24 hours with DMSO, 250 nM rapamycin or 500 nM CCT020312. Main lipid classes were solvent extracted from whole cell lysate and quantified relative to compound treatment. Results are represented as normalized intensity relative to DMSO mean ± SD (n = 4 biological replicates). * Holm multiple comparison test following one-way ANOVA $p < .05$, ** $p < .01$, *** $p < .005$. (**D**-**E**) Volcano plots depicting -$\log_{10}$(p-value) and $\log_2$(fold change) for tandem mass spectrometry results of HEK293T cells treated with (**D**) 250 nM rapamycin or (**E**) 500 nM, 1 µM or 2.5 µM CCT020312 for 24 hours. (**F**-**G**) Volcano plots depicting -$\log_{10}$(p-value) and $\log_2$(fold change) for phosphoproteomics results of HEK293T cells treated with (**F**) 250 nM rapamycin or (**G**) 500 nM, 1 µM or 2.5 µM CCT020312 for 24 hours.

Figure 5: CCT020312 clears PrP^{PG14} aggregates in primary mouse hippocampal neurons. (**A**) Left: representative images of axons of neurons expressing PrP^{WT}-mCh or PrP^{PG14}-mCh treated with CCT020312 or DMSO (vehicle). Right: axonal aggregate density quantification showing a

statistically significant, dose-dependent decrease in axonal aggregate density starting at 50 nM CCT020312. (**B**) Left: representative images of axons of neurons expressing PrP^{WT}-mCh or PrP^{PG14}-mCh treated with carboxy-CCT or DMSO. Right: axonal aggregate density quantification showing no statistically significant decrease in axonal aggregate density. *p < .05, ** p < .01, *** p < .001, **** p < .0001, ns = not statistically significant. One-way ANOVA, Šidák correction. (**C**) Representative kymographs of axonal transport in neurons expressing PrP^{WT}-mCh or PrP^{PG14}-mCh treated with CCT020312 or DMSO. (**D**) Cumulative frequency distribution of anterograde and retrograde segmental velocities (top) and segmental run lengths (bottom) from PrP^{WT}-mCh or PrP^{PG14}-mCh vesicles in axons expressing PrP^{WT}-mCh or PrP^{PG14}-mCh treated with CCT020312 or DMSO (vehicle). * Kolmogorov-Smirnov p < .05, ** p < .01, *** p < .001, ns = not statistically significant. (**E**) Pause frequency (left) and density (right) of PrP^{WT}-mCh or PrP^{PG14}-mCh vesicles in axons expressing PrP^{WT}-mCh or PrP^{PG14}-mCh treated with CCT020312 or DMSO (vehicle). * Dunn's multiple comparison test following Kruskal-Wallis p < .05, ** p < .01, *** p < .001, **** p < .0001, ns = not statistically significant.

Figure 6: CCT020312 rescues tauopathy phenotypes in FTD patient iPSC-derived tau-P301L neurons. (**A**) CCT020312 concentration effect on total tau (TAU5) and P-tau S396 and S202/T205 (AT8) of P301L neurons after 24 hrs treatment. Detection of monomeric (~55 kDa) and high MW oligomeric (≥250 kDa) P-tau S396. Brackets depict bands used for densitometry analysis in (**B**). (**B**) Western blot densitometry, quantification of bands' pixel intensity (in arbitrary units, a.u.). Data points represent mean densitometry normalized to actin and relative to vehicle (DMSO) ± SD (*n* = 2). (**C, D**) CCT020312 effect on tau solubility in P301L neurons. Western blot (**C**) and densitometry (**D**) quantification of total tau (TAU5), P-tau S396 and P-tau S202/T205 (AT8) in the soluble (S) and insoluble-pellet (P) fractions of neurons treated for 24 hrs. Brackets (C) indicate the bands used for analysis in (**D**). Graph bars represent mean densitometry ± SD (*n* =2) for soluble (*left*) and insoluble (*right*) tau levels relative to vehicle samples (0 μM, DMSO). (**E, F**) Single 24h dose of CCT020312 has a prolonged effect on tau reduction. Tau-P301L neurons were treated for 24 hrs, followed by compound washout (red arrow). Total tau and P-tau were measured by western blot (**E**) over a period of 16 days post-treatment. Graph data points (**F**) represent mean densitometry (bands within brackets) ± SD (*n* = 2), relative to day 0/Vehicle DMSO. β-III tubulin served as a control for neuronal integrity during the time-course. (**G**) Rescue of stress vulnerability in a tauopathy neuronal model by CCT020312. The stressors rotenone (*top*), NMDA (*center*) and Aβ (1-42) (*bottom*) reveal P301L neuronal stress vulnerability by causing ~60-90% loss in viability. Pre-treatment with 1 μM or 10 μM CCT020312 rescued neuronal viability to 60-100% of vehicle (DMSO). Graph bars represent mean viability relative to vehicle-treated neurons (100%) ± SD (*n* = 2, and four technical replicates). Two-tailed unpaired Student's T-test ^{ns}p > .05; *p < .05, **p < .01, ***p < .001. (**H**) Fluorescence imaging of tau-P301L neurons treated with vehicle (DMSO) or 1 μM CCT020312, (immuno-)probed for LysoTracker red, P-tau PHF-1 (red), LAMP1 (red) and the neuronal marker MAP2 (green). White arrows point to accumulation of LysoTracker (ii) and LAMP1 (vi) in the cell body of neurons treated with CCT020312. Insets show zoomed images of the dotted boxes.

Figure 7: CCT020312 reduces Aβ and Aβ (1-42) peptide levels in AD-patient iNS. Quantification of mean fluorescence intensity of **(A)** total amyloid beta (Aβ) and **(B)** the aggregation-prone peptide species, Aβ(1-42), in the cell body of directly induced neurons (iNs)

from fibroblasts of patients with sporadic Alzheimer's disease (sAD) or AD carrying PSEN1 A431E mutation (AD-PSEN1). Treatment of 1 μM BACE-1 inhibitor (β-Secretase Inhibitor IV, Sigma-Aldrich), 250 nM Rapamycin and CCT020312 ranging from 125, 250 and 500 nM for 48 hours. Statistical analysis was performed with one-way ANOVA and Bonferroni's post hoc test. ***$p < 0.001$ (vs. DMSO). Experiments were repeated three times. Data represented as box-and-whisker plots.

Figure 1.

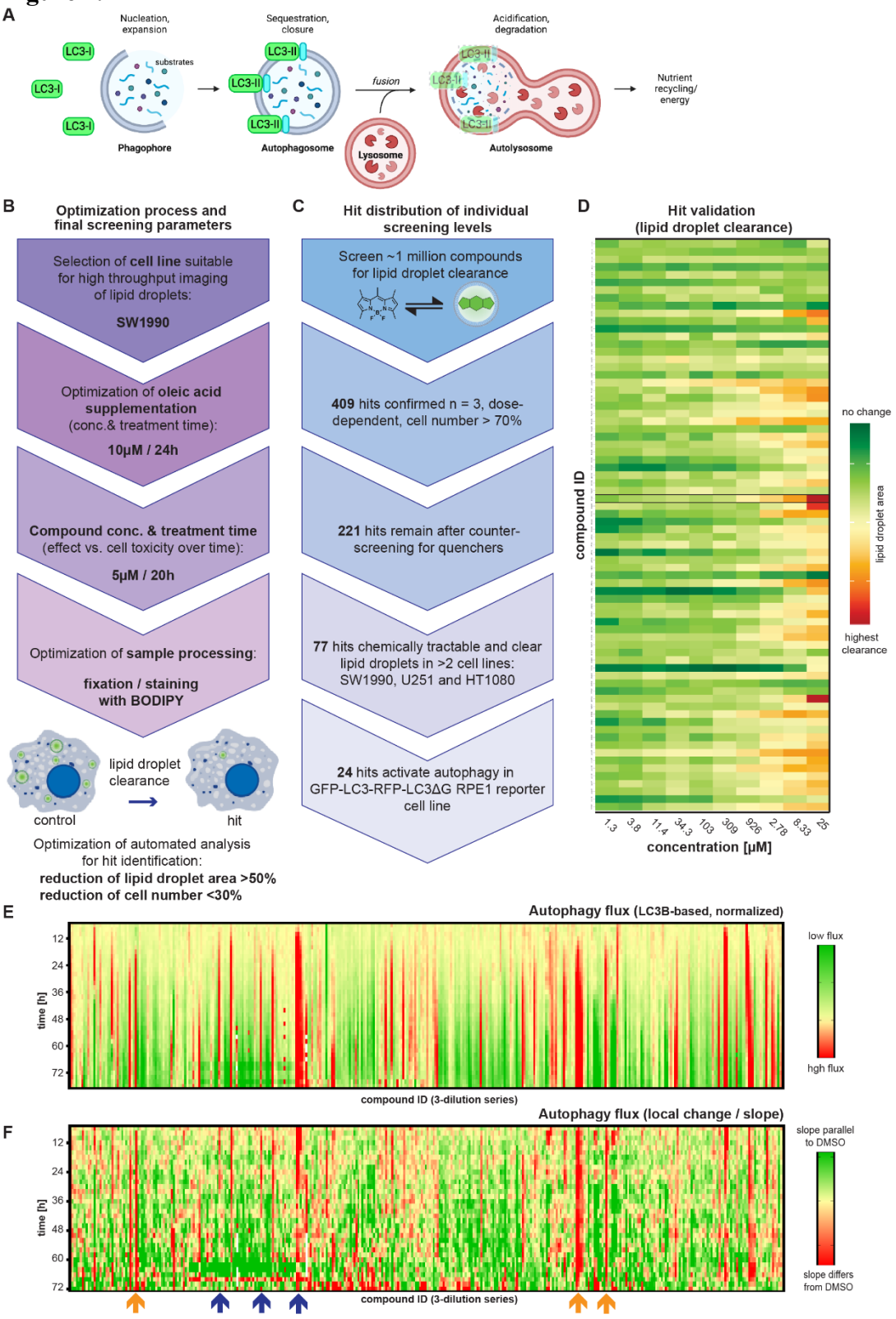
A
Nucleation, expansion
Sequestration, closure
Acidification, degradation
LC3-I
substrates
LC3-II
fusion
Lysosome
Nutrient recycling/ energy
Phagophore
Autophagosome
Autolysosome
B
Optimization process and final screening parameters
Selection of cell line suitable for high throughput imaging of lipid droplets:
SW1990
Optimization of oleic acid supplementation (conc.& treatment time):
10µM / 24h
Compound conc. & treatment time (effect vs. cell toxicity over time):
5µM / 20h
Optimization of sample processing:
fixation / staining with BODIPY
lipid droplet clearance
control
hit
Optimization of automated analysis for hit identification:
reduction of lipid droplet area >50%
reduction of cell number <30%
C
Hit distribution of individual screening levels
Screen ~1 million compounds for lipid droplet clearance
409 hits confirmed n = 3, dose-dependent, cell number > 70%
221 hits remain after counter-screening for quenchers
77 hits chemically tractable and clear lipid droplets in >2 cell lines: SW1990, U251 and HT1080
24 hits activate autophagy in GFP-LC3-RFP-LC3ΔG RPE1 reporter cell line
D
Hit validation (lipid droplet clearance)
compound ID
no change
lipid droplet area
highest clearance
1.3
3.8
11.4
34.3
103
309
926
2.78
8.33
25
concentration [µM]
E
Autophagy flux (LC3B-based, normalized)
time [h]
12
24
36
48
60
72
compound ID (3-dilution series)
low flux
hgh flux
F
Autophagy flux (local change / slope)
time [h]
12
24
36
48
60
72
compound ID (3-dilution series)
slope parallel to DMSO
slope differs from DMSO

Figure 2.

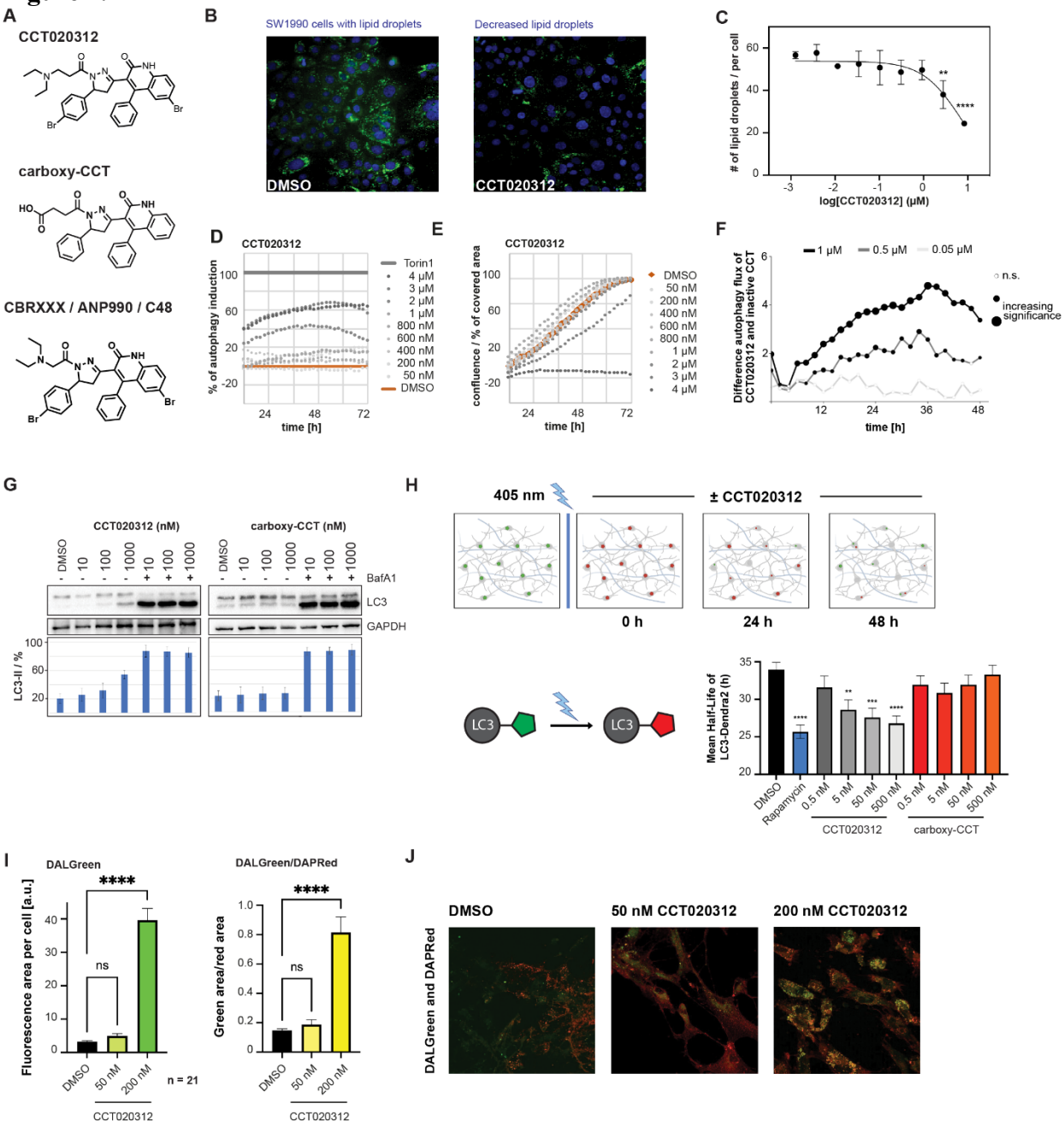
A
CCT020312
carboxy-CCT
CBRXXX / ANP990 / C48
B
SW1990 cells with lipid droplets
Decreased lipid droplets
DMSO
CCT020312
C
# of lipid droplets / per cell
log[CCT020312] (µM)
D
CCT020312
% of autophagy induction
time [h]
Torin1
4 µM
3 µM
2 µM
1 µM
800 nM
600 nM
400 nM
200 nM
50 nM
DMSO
E
CCT020312
confluence / % of covered area
time [h]
DMSO
50 nM
200 nM
400 nM
600 nM
800 nM
1 µM
2 µM
3 µM
4 µM
F
1 µM
0.5 µM
0.05 µM
n.s.
increasing significance
Difference autophagy flux of CCT020312 and inactive CCT
time [h]
G
CCT020312 (nM)
carboxy-CCT (nM)
DMSO
BafA1
LC3
GAPDH
LC3-II / %
H
405 nm
± CCT020312
0 h
24 h
48 h
LC3
Mean Half-Life of LC3-Dendra2 (h)
DMSO
Rapamycin
0.5 nM
5 nM
50 nM
500 nM
CCT020312
carboxy-CCT
I
DALGreen
Fluorescence area per cell [a.u.]
ns
****
n = 21
DMSO
50 nM
200 nM
CCT020312
DALGreen/DAPRed
Green area/red area
J
DMSO
50 nM CCT020312
200 nM CCT020312
DALGreen and DAPRed

Figure 3.

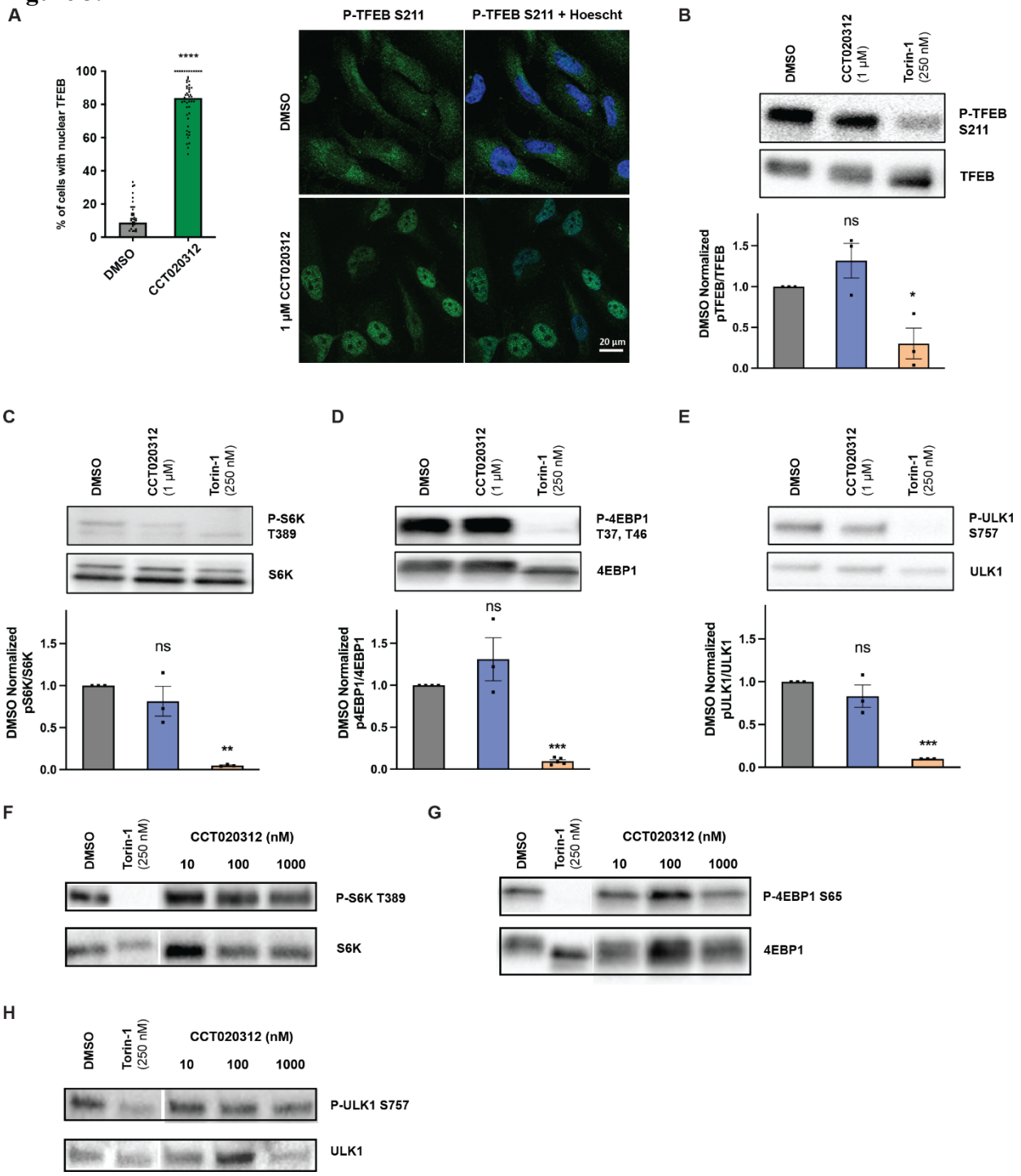
A
P-TFEB S211
P-TFEB S211 + Hoescht
DMSO
1 µM CCT020312
20 µm
% of cells with nuclear TFEB
****
DMSO
CCT020312
B
DMSO
CCT020312 (1 µM)
Torin-1 (250 nM)
P-TFEB S211
TFEB
DMSO Normalized pTFEB/TFEB
ns
*
C
P-S6K T389
S6K
DMSO Normalized pS6K/S6K
ns
**
D
P-4EBP1 T37, T46
4EBP1
DMSO Normalized p4EBP1/4EBP1
ns
***
E
P-ULK1 S757
ULK1
DMSO Normalized pULK1/ULK1
ns
***
F
CCT020312 (nM)
10
100
1000
P-S6K T389
S6K
G
P-4EBP1 S65
4EBP1
H
P-ULK1 S757
ULK1

Figure 4.

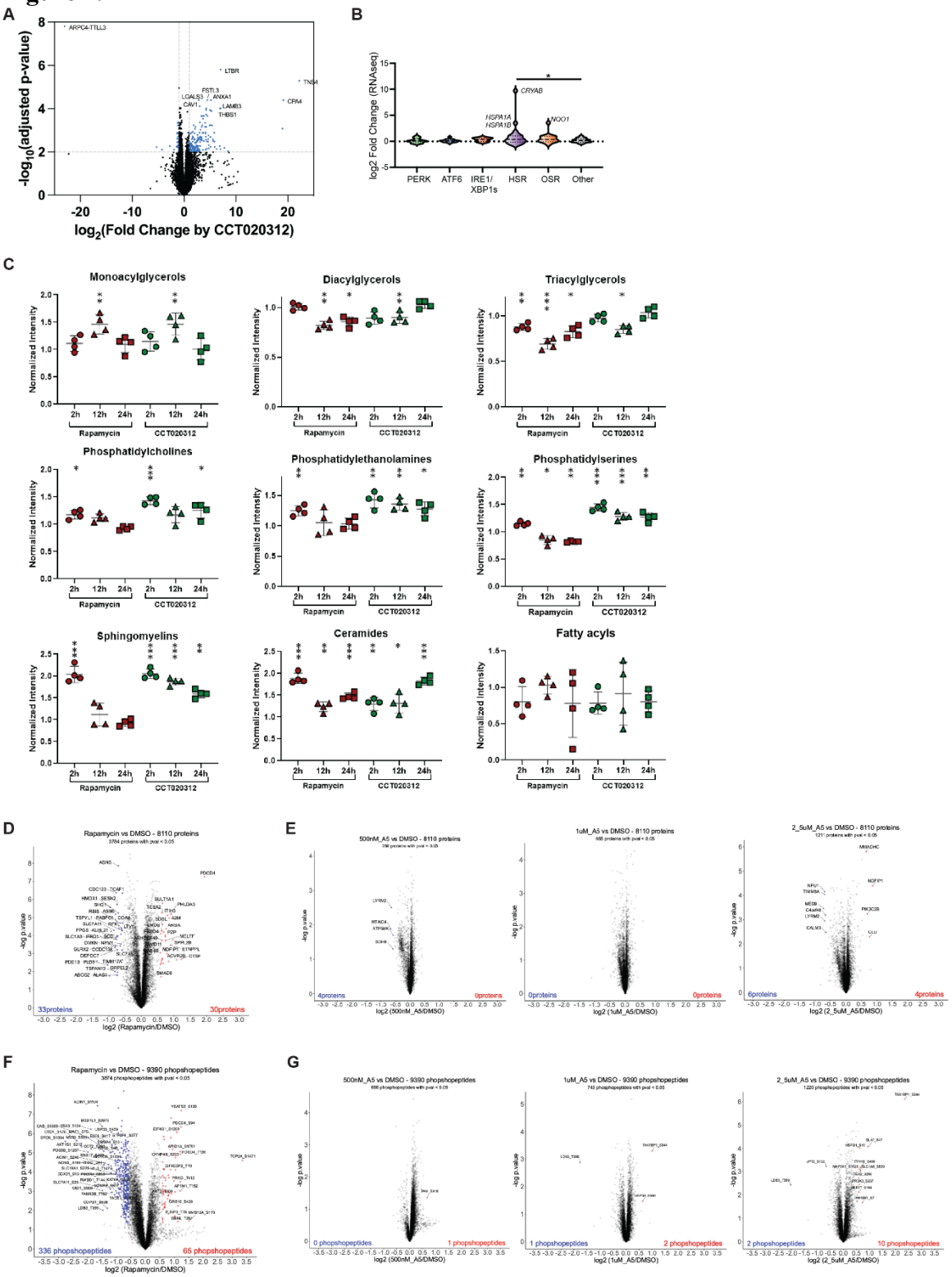
A
-log10(adjusted p-value)
log2(Fold Change by CCT020312)
ARPC4-TTLL3
LTBR
TNS4
CPA4
FSTL3
LGALS3
ANXA1
CAV1
LAMB3
THBS1
B
log2 Fold Change (RNAseq)
CRYAB
HSPA1A
HSPA1B
NQO1
PERK
ATF6
IRE1/ XBP1s
HSR
OSR
Other
C
Monoacylglycerols
Diacylglycerols
Triacylglycerols
Phosphatidylcholines
Phosphatidylethanolamines
Phosphatidylserines
Sphingomyelins
Ceramides
Fatty acyls
Normalized Intensity
2h
12h
24h
Rapamycin
CCT020312
D
Rapamycin vs DMSO - 8110 proteins
3784 proteins with pval < 0.05
-log p value
log2 (Rapamycin/DMSO)
33proteins
30proteins
E
500nM_A5 vs DMSO - 8110 proteins
1uM_A5 vs DMSO - 8110 proteins
2_5uM_A5 vs DMSO - 8110 proteins
4proteins
0proteins
0proteins
0proteins
6proteins
4proteins
log2 (500nM_A5/DMSO)
log2 (1uM_A5/DMSO)
log2 (2_5uM_A5/DMSO)
F
Rapamycin vs DMSO - 9390 phopshopeptides
3874 phosphopeptides with pval < 0.05
336 phosphopeptides
65 phosphopeptides
G
500nM_A5 vs DMSO - 9390 phopshopeptides
1uM_A5 vs DMSO - 9390 phopshopeptides
2_5uM_A5 vs DMSO - 9390 phopshopeptides
0 phosphopeptides
1 phosphopeptides
1 phosphopeptides
2 phosphopeptides
2 phosphopeptides
10 phosphopeptides

Figure 5.

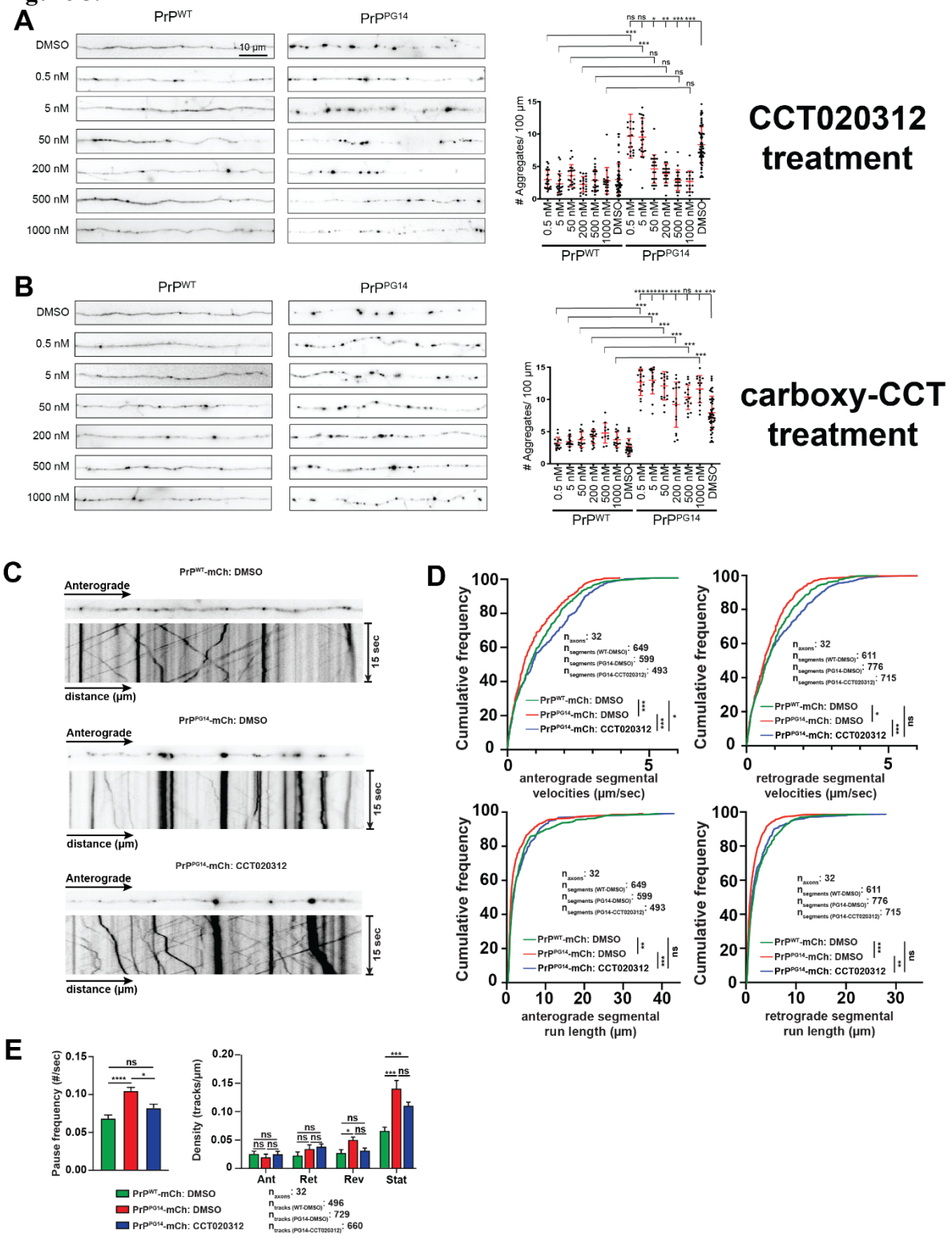
A
PrP^WT
PrP^PG14
DMSO
0.5 nM
5 nM
50 nM
200 nM
500 nM
1000 nM
10 µm
Aggregates/ 100 µm
CCT020312 treatment
B
carboxy-CCT treatment
C
PrP^WT-mCh: DMSO
PrP^PG14-mCh: DMSO
PrP^PG14-mCh: CCT020312
Anterograde
distance (µm)
15 sec
D
Cumulative frequency
anterograde segmental velocities (µm/sec)
retrograde segmental velocities (µm/sec)
anterograde segmental run length (µm)
retrograde segmental run length (µm)
n_axons: 32
n_segments (WT-DMSO): 649
n_segments (PG14-DMSO): 599
n_segments (PG14-CCT020312): 493
n_segments (WT-DMSO): 611
n_segments (PG14-DMSO): 776
n_segments (PG14-CCT020312): 715
E
Pause frequency (#/sec)
Density (tracks/µm)
Ant
Ret
Rev
Stat
n_axons: 32
n_tracks (WT-DMSO): 496
n_tracks (PG14-DMSO): 729
n_tracks (PG14-CCT020312): 660

Figure 6.

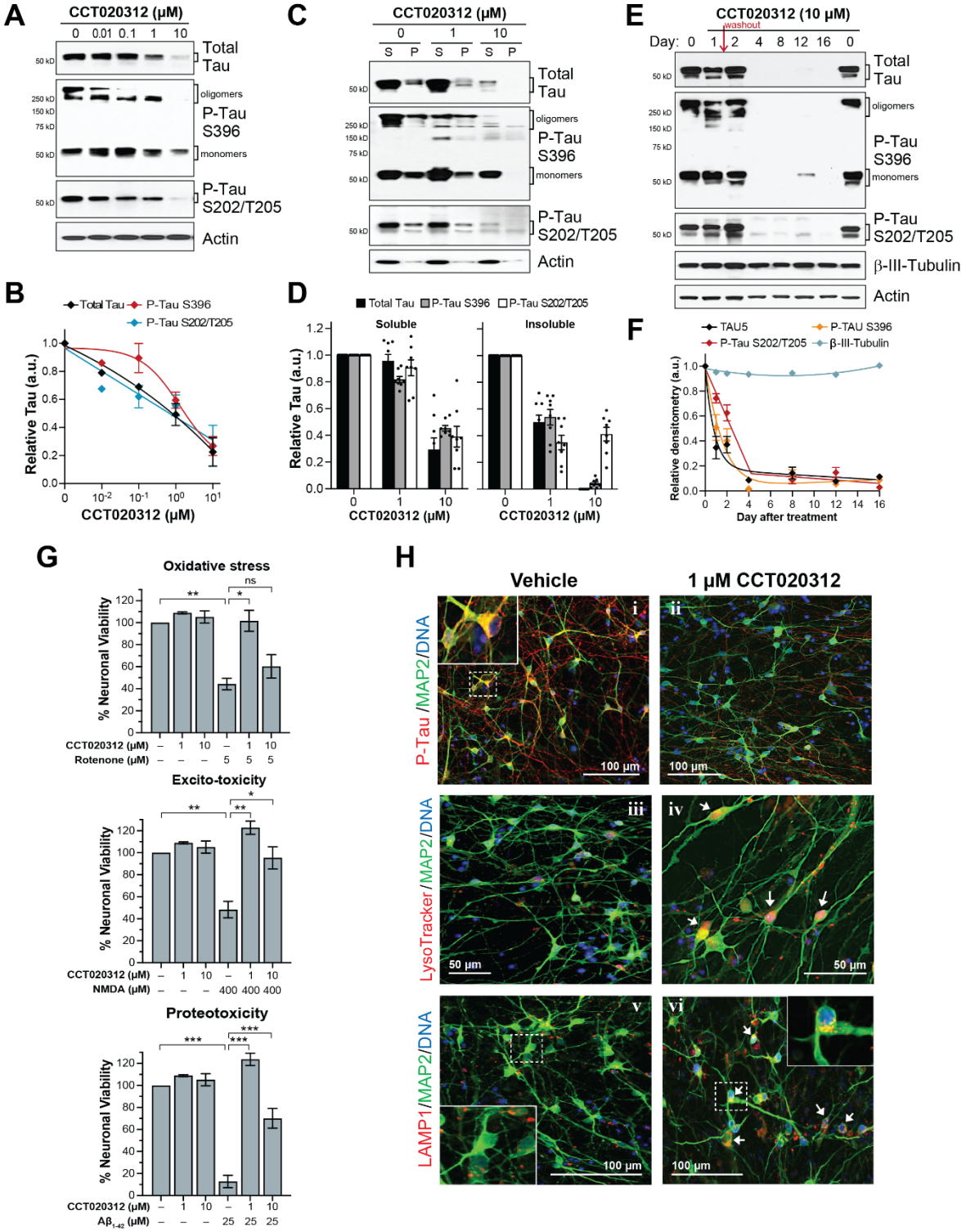
A
CCT020312 (μM)
0 0.01 0.1 1 10
Total Tau
oligomers
P-Tau S396
monomers
P-Tau S202/T205
Actin
B
Total Tau
P-Tau S396
P-Tau S202/T205
Relative Tau (a.u.)
CCT020312 (μM)
C
CCT020312 (μM)
0 1 10
S P S P S P
Total Tau
oligomers
P-Tau S396
monomers
P-Tau S202/T205
Actin
D
Total Tau
P-Tau S396
P-Tau S202/T205
Soluble
Insoluble
Relative Tau (a.u.)
CCT020312 (μM)
E
CCT020312 (10 μM)
washout
Day: 0 1 2 4 8 12 16 0
Total Tau
oligomers
P-Tau S396
monomers
P-Tau S202/T205
β-III-Tubulin
Actin
F
TAU5
P-TAU S396
P-Tau S202/T205
β-III-Tubulin
Relative densitometry (a.u.)
Day after treatment
G
Oxidative stress
% Neuronal Viability
CCT020312 (μM)
Rotenone (μM)
Excito-toxicity
NMDA (μM)
Proteotoxicity
Aβ1-42 (μM)
H
Vehicle
1 μM CCT020312
P-Tau /MAP2/DNA
LysoTracker / MAP2/DNA
LAMP1/MAP2/DNA
100 μm
50 μm

Figure 7.

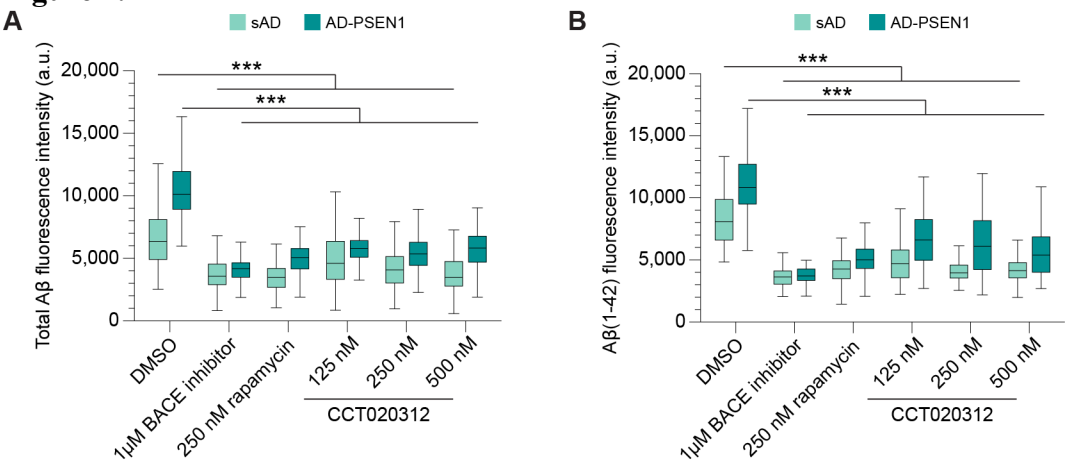
A
sAD
AD-PSEN1
Total Aβ fluorescence intensity (a.u.)
20,000
15,000
10,000
5,000
0
***
***
DMSO
1μM BACE inhibitor
250 nM rapamycin
125 nM
250 nM
500 nM
CCT020312
B
sAD
AD-PSEN1
Aβ(1-42) fluorescence intensity (a.u.)
20,000
15,000
10,000
5,000
0
***
***
DMSO
1μM BACE inhibitor
250 nM rapamycin
125 nM
250 nM
500 nM
CCT020312

References

Al-Bari, M.A.A., and Xu, P.Y. (2020). Molecular regulation of autophagy machinery by mTOR-dependent and -independent pathways. Annals of the New York Academy of Sciences *1467*, 3-20. 10.1111/nyas.14305.

Alquezar, C., Schoch, K.M., Geier, E.G., Ramos, E.M., Scrivo, A., Li, K.H., Argouarch, A.R., Mlynarski, E.E., Dombroski, B., DeTure, M., et al. (2021). TSC1 loss increases risk for tauopathy by inducing tau acetylation and preventing tau clearance via chaperone-mediated autophagy. Sci. Adv. *7*, 15, eabg3897. 10.1126/sciadv.abg3897.

An, H., and Harper, J.W. (2018). Systematic analysis of ribophagy in human cells reveals bystander flux during selective autophagy. Nature Cell Biology *20*, 135-+. 10.1038/s41556-017-0007-x.

An, H., Ordureau, A., Paulo, J.A., Shoemaker, C.J., Denic, V., and Harper, J.W. (2019). TEX264 Is an Endoplasmic Reticulum-Resident ATG8-Interacting Protein Critical for ER Remodeling during Nutrient Stress. Molecular Cell *74*, 891-+. 10.1016/j.molcel.2019.03.034.

Axten, J.M., Romeril, S.P., Shu, A., Ralph, J., Medina, J.R., Feng, Y., Li, W.H., Grant, S.W., Heerding, D.A., Minthorn, E., et al. (2013). Discovery of GSK2656157: An Optimized PERK Inhibitor Selected for Preclinical Development. ACS Med Chem Lett *4*, 964-968. 10.1021/ml400228e.

Balgi, A.D., Fonseca, B.D., Donohue, E., Tsang, T.C.F., Lajoie, P., Proud, C.G., Nabi, I.R., and Roberge, M. (2009). Screen for Chemical Modulators of Autophagy Reveals Novel Therapeutic Inhibitors of mTORC1 Signaling. Plos One *4*, e7124. 10.1371/journal.pone.0007124.

Bligh, E.G., and Dyer, W.J. (1959). A rapid method of total lipid extraction and purification. Can J Biochem Physiol *37*, 911-917. 10.1139/o59-099.

Borchelt, D.R., Davis, J., Fischer, M., Lee, M.K., Slunt, H.H., Ratovitsky, T., Regard, J., Copeland, N.G., Jenkins, N.A., Sisodia, S.S., and Price, D.L. (1996). A vector for expressing foreign genes in the brains and hearts of transgenic mice. Genetic Analysis: Biomolecular Engineering *13*, 159-163. https://doi.org/10.1016/S1050-3862(96)00167-2.

Bourdenx, M., Martín-Segura, A., Scrivo, A., Rodriguez-Navarro, J.A., Kaushik, S., Tasset, I., Diaz, A., Storm, N.J., Xin, Q., Juste, Y.R., et al. (2021). Chaperone-mediated autophagy prevents collapse of the neuronal metastable proteome. Cell *184*, 2696-2714.e2625. 10.1016/j.cell.2021.03.048.

Brady, O.A., Zheng, Y.Q., Murphy, K., Huang, M., and Hu, F.H. (2013). The frontotemporal lobar degeneration risk factor, TMEM106B, regulates lysosomal morphology and function. Human Molecular Genetics *22*, 685-695. 10.1093/hmg/dds475.

Bruch, J., Xu, H., Rosler, T.W., De Andrade, A., Kuhn, P.H., Lichtenthaler, S.F., Arzberger, T., Winklhofer, K.F., Muller, U., and Huglinger, G.U. (2017). PERK activation mitigates tau

pathology in vitro and in vivo. Embo Molecular Medicine *9*, 371-384. 10.15252/emmm.201606664.

Bucci, C., Thomsen, P., Nicoziani, P., McCarthy, J., and van Deurs, B. (2000). Rab7: a key to lysosome biogenesis. Mol Biol Cell *11*, 467-480. 10.1091/mbc.11.2.467.

Butlers, V.J., Cortopassi, W.A., Argouarch, A.R., Ivry, S.L., Craik, C.S., Jacobson, M.P., and Kao, A.W. (2019). Progranulin Stimulates the In Vitro Maturation of Pro-Cathepsin D at Acidic pH. Journal of Molecular Biology *431*, 1038-1047. 10.1016/j.jmb.2019.01.027.

Chambers, M.C., Maclean, B., Burke, R., Amodei, D., Ruderman, D.L., Neumann, S., Gatto, L., Fischer, B., Pratt, B., Egertson, J., et al. (2012). A cross-platform toolkit for mass spectrometry and proteomics. Nat Biotechnol *30*, 918-920. 10.1038/nbt.2377.

Chang, J., Lee, S., and Blackstone, C. (2014). Spastic paraplegia proteins spastizin and spatacsin mediate autophagic lysosome reformation. Journal of Clinical Investigation *124*, 5249-5262. 10.1172/jci77598.

Chassefeyre, R., Chaiamarit, T., Verhelle, A., Novak, S.W., Andrade, L.R., Leitao, A.D.G., Manor, U., and Encalada, S.E. (2021). Endosomal sorting drives the formation of axonal prion protein endoggresomes. Sci. Adv. *7*, 20, eabg3693. 10.1126/sciadv.abg3693.

Chauhan, S., Ahmed, Z., Bradfute, S.B., Arko-Mensah, J., Mandell, M.A., Choi, S.W., Kimura, T., Blanchet, F., Waller, A., Mudd, M.H., et al. (2015). Pharmaceutical screen identifies novel target processes for activation of autophagy with a broad translational potential. Nature Communications *6*, 8620. 10.1038/ncomms9620.

Cherry, S., Jin, E.J., Ozel, M.N., Lu, Z., Agi, E., Wang, D., Jung, W.H., Epstein, D., Meinertzhagen, I.A., Chan, C.C., and Hiesinger, P.R. (2013). Charcot-Marie-Tooth 2B mutations in rab7 cause dosage-dependent neurodegeneration due to partial loss of function. eLife *2*, e01064. 10.7554/eLife.01064.

Chin, M.Y., Ang, K.H., Davies, J., Alquezar, C., Garda, V.G., Rooney, B., Leng, K., Kampmann, M., Arkin, M.R., and Kao, A.W. (2022). Phenotypic Screening Using High-Content Imaging to Identify Lysosomal pH Modulators in a Neuronal Cell Model. ACS Chem. Neurosci. *13*, 1505-1516. 10.1021/acschemneuro.1c00804.

Cingolani, F., and Czaja, M.J. (2016). Regulation and Functions of Autophagic Lipolysis. Trends Endocrinol Metab *27*, 696-705. 10.1016/j.tem.2016.06.003.

Clayton, E.L., Mizielinska, S., Edgar, J.R., Nielsen, T.T., Marshall, S., Norona, F.E., Robbins, M., Damirji, H., Holm, I.E., Johannsen, P., et al. (2015). Frontotemporal dementia caused by CHMP2B mutation is characterised by neuronal lysosomal storage pathology. Acta Neuropathologica *130*, 511-523. 10.1007/s00401-015-1475-3.

Cotman, S.L., Karaa, A., Staropoli, J.F., and Sims, K.B. (2013). Neuronal Ceroid Lipofuscinosis: Impact of Recent Genetic Advances and Expansion of the Clinicopathologic Spectrum. Curr. Neurol. Neurosci. Rep. *13*, 11, 366. 10.1007/s11910-013-0366-z.

Crother, T.R., Porritt, R.A., Dagvadorj, J., Tumurkhuu, G., Slepenkin, A.V., Peterson, E.M., Chen, S., Shimada, K., and Arditi, M. (2019). Autophagy Limits Inflammasome During Chlamydia pneumoniae Infection. Frontiers in Immunology *10*, 11, 754. 10.3389/fimmu.2019.00754.

Daniele, S., Sestito, S., Pietrobono, D., Giacomelli, C., Chiellini, G., Di Maio, D., Marinelli, L., Novellino, E., Martini, C., and Rapposelli, S. (2017). Dual Inhibition of PDK1 and Aurora Kinase A: An Effective Strategy to Induce Differentiation and Apoptosis of Human Glioblastoma Multiforme Stem Cells. ACS Chem Neurosci *8*, 100-114. 10.1021/acschemneuro.6b00251.

Dodson, M., Redmann, M., Rajasekaran, N.S., Darley-Usmar, V., and Zhang, J. (2015). KEAP1-NRF2 signalling and autophagy in protection against oxidative and reductive proteotoxicity. Biochem J *469*, 347-355. 10.1042/bj20150568.

Duan, L.S., Hu, M.F., Tamm, J.A., Grinberg, Y.Y., Shen, F., Chai, Y.T., Xi, H.L., Gibilisco, L., Ravikumar, B., Gautam, V., et al. (2021). Arrayed CRISPR reveals genetic regulators of tau aggregation, autophagy and mitochondria in Alzheimer's disease model. Scientific Reports *11*, 17, 2879. 10.1038/s41598-021-82658-7.

Eapen, V.V., Swarup, S., Hoyer, M.J., Paulo, J.A., and Harper, J.W. (2021). Quantitative proteomics reveals the selectivity of ubiquitin-binding autophagy receptors in the turnover of damaged lysosomes by lysophagy. eLife *10*, 36, e72328. 10.7554/eLife.72328; 10.7554/eLife.72328.sa1; 10.7554/eLife.72328.sa2.

Encalada, S.E., Szpankowski, L., Xia, C.H., and Goldstein, L.S.B. (2011). Stable Kinesin and Dynein Assemblies Drive the Axonal Transport of Mammalian Prion Protein Vesicles. Cell *144*, 551-565. 10.1016/j.cell.2011.01.021.

Fernández Á, F., Sebti, S., Wei, Y., Zou, Z., Shi, M., McMillan, K.L., He, C., Ting, T., Liu, Y., Chiang, W.C., et al. (2018). Disruption of the beclin 1-BCL2 autophagy regulatory complex promotes longevity in mice. Nature *558*, 136-140. 10.1038/s41586-018-0162-7.

Freischmidt, A., Wieland, T., Richter, B., Ruf, W., Schaeffer, V., Müller, K., Marroquin, N., Nordin, F., Hübers, A., Weydt, P., et al. (2015). Haploinsufficiency of TBK1 causes familial ALS and fronto-temporal dementia. Nature Neuroscience *18*, 631-636. 10.1038/nn.4000.

Ganz, J., Shacham, T., Kramer, M., Shenkman, M., Eiger, H., Weinberg, N., Iancovici, O., Roy, S., Simhaev, L., Da'adoosh, B., et al. (2020). A novel specific PERK activator reduces toxicity and extends survival in Huntington's disease models. Scientific Reports *10*, 15, 6875. 10.1038/s41598-020-63899-4.

Gingras, A.C., Raught, B., and Sonenberg, N. (2001). Regulation of translation initiation by FRAP/mTOR. Genes Dev *15*, 807-826. 10.1101/gad.887201.

Goodall, E.A., Kraus, F., and Harper, J.W. (2022). Mechanisms underlying ubiquitin-driven selective mitochondrial and bacterial autophagy. Molecular Cell *82*, 1501-1513. 10.1016/j.molcel.2022.03.012.

Grandl, M., and Schmitz, G. (2010). Fluorescent High-Content Imaging Allows the Discrimination and Quantitation of E-LDL-Induced Lipid Droplets and Ox-LDL-Generated Phospholipidosis in Human Macrophages. Cytometry Part A *77A*, 231-242. 10.1002/cyto.a.20828.

Guo, J.L., and Lee, V.M. (2011). Seeding of normal Tau by pathological Tau conformers drives pathogenesis of Alzheimer-like tangles. J Biol Chem *286*, 15317-15331. 10.1074/jbc.M110.209296.

Hara, T., Nakamura, K., Matsui, M., Yamamoto, A., Nakahara, Y., Suzuki-Migishima, R., Yokoyama, M., Mishima, K., Saito, I., Okano, H., and Mizushima, N. (2006). Suppression of basal autophagy in neural cells causes neurodegenerative disease in mice. Nature *441*, 885-889. 10.1038/nature04724.

Harold, D., Abraham, R., Hollingworth, P., Sims, R., Gerrish, A., Hamshere, M.L., Pahwa, J.S., Moskvina, V., Dowzell, K., Williams, A., et al. (2009). Genome-wide association study identifies variants at CLU and PICALM associated with Alzheimer's disease. Nature Genetics *41*, 1088-U1061. 10.1038/ng.440.

Hou, Y., Dan, X., Babbar, M., Wei, Y., Hasselbalch, S.G., Croteau, D.L., and Bohr, V.A. (2019). Ageing as a risk factor for neurodegenerative disease. Nat Rev Neurol *15*, 565-581. 10.1038/s41582-019-0244-7.

Ichimura, Y., Kirisako, T., Takao, T., Satomi, Y., Shimonishi, Y., Ishihara, N., Mizushima, N., Tanida, I., Kominami, E., Ohsumi, M., et al. (2000). A ubiquitin-like system mediates protein lipidation. Nature *408*, 488-492. 10.1038/35044114.

Iwashita, H., Sakurai, H.T., Nagahora, N., Ishiyama, M., Shioji, K., Sasamoto, K., Okuma, K., Shimizu, S., and Ueno, Y. (2018). Small fluorescent molecules for monitoring autophagic flux. FEBS Letters *592*, 559-567. https://doi.org/10.1002/1873-3468.12979.

Jiang, Y., Sato, Y., Im, E., Berg, M., Bordi, M., Darji, S., Kumar, A., Mohan, P.S., Bandyopadhyay, U., Diaz, A., et al. (2019). Lysosomal Dysfunction in Down Syndrome Is APP-Dependent and Mediated by APP-beta CTF (C99). Journal of Neuroscience *39*, 5255-5268. 10.1523/jneurosci.0578-19.2019.

Jin, S.M., and Youle, R.J. (2012). PINK1- and Parkin-mediated mitophagy at a glance. J Cell Sci *125*, 795-799. 10.1242/jcs.093849.

Kabeya, Y., Mizushima, N., Uero, T., Yamamoto, A., Kirisako, T., Noda, T., Kominami, E., Ohsumi, Y., and Yoshimori, T. (2000). LC3, a mammalian homologue of yeast Apg8p, is localized in autophagosome membranes after processing. Embo Journal *19*, 5720-5728. 10.1093/emboj/19.21.5720.

Kaizuka, T., Morishita, H., Hama, Y., Tsukamoto, S., Matsui, T., Toyota, Y., Kodama, A., Ishihara, T., Mizushima, T., and Mizushima, N. (2016). An Autophagic Flux Probe that Releases an Internal Control. Molecular Cell *64*, 835-849. 10.1016/j.molcel.2016.09.037.

Kao, A.W., McKay, A., Singh, P.P., Brunet, A., and Huang, E.J. (2017). Progranulin, lysosomal regulation and neurodegenerative disease. Nature Reviews Neuroscience *18*, 325-333. 10.1038/nrn.2017.36.

Kfoury, N., Holmes, B.B., Jiang, H., Holtzman, D.M., and Diamond, M.I. (2012). Trans-cellular propagation of Tau aggregation by fibrillar species. J Biol Chem *287*, 19440-19451. 10.1074/jbc.M112.346072.

Khaminets, A., Heinrich, T., Mari, M., Grumati, P., Huebner, A.K., Akutsu, M., Liebmann, L., Stolz, A., Nietzsche, S., Koch, N., et al. (2015). Regulation of endoplasmic reticulum turnover by selective autophagy. Nature *522*, 354-+. 10.1038/nature14498.

Kim, E., Lee, S., and Park, S.B. (2012). A Seoul-Fluor-based bioprobe for lipid droplets and its application in image-based high throughput screening. Chemical Communications *48*, 2331-2333. 10.1039/c2cc17496k.

Kim, J., Kundu, M., Viollet, B., and Guan, K.L. (2011). AMPK and mTOR regulate autophagy through direct phosphorylation of Ulk1. Nat Cell Biol. *13*, 132-141. 10.1038/ncb2152.
Kim, Y.C., and Guan, K.L. (2015). mTOR: a pharmacologic target for autophagy regulation. J Clin Invest *125*, 25-32. 10.1172/jci73939.

Kimura, S., Noda, T., and Yoshimori, T. (2007). Dissection of the autophagosome maturation process by a novel reporter protein, tandem fluorescent-tagged LC3. Autophagy *3*, 452-460. 10.4161/auto.4451.

Kirkin, V., McEwan, D.G., Novak, I., and Dikic, I. (2009). A Role for Ubiquitin in Selective Autophagy. Molecular Cell *34*, 259-269. 10.1016/j.molcel.2009.04.026.

Klionsky, D.J., Abdel-Aziz, A.K., Abdelfatah, S., Abdellatif, M., Abdoli, A., Abel, S., Abeliovich, H., Abildgaard, M.H., Abudu, Y.P., Acevedo-Arozena, A., et al. (2021). Guidelines for the use and interpretation of assays for monitoring autophagy (4th edition)(1). Autophagy *17*, 1-382. 10.1080/15548627.2020.1797280.

Klionsky, D.J., Abdelmohsen, K., Abe, A., Abedin, M.J., Abeliovich, H., Acevedo Arozena, A., Adachi, H., Adams, C.M., Adams, P.D., Adeli, K., et al. (2016). Guidelines for the use and interpretation of assays for monitoring autophagy (3rd edition). Autophagy *12*, 1-222. 10.1080/15548627.2015.1100356.

Komatsu, M., Waguri, S., Chiba, T., Murata, S., Iwata, J., Tanida, I., Ueno, T., Koike, M., Uchiyama, Y., Kominami, E., and Tanaka, K. (2006). Loss of autophagy in the central nervous system causes neurodegeneration in mice. Nature *441*, 880-884. 10.1038/nature04723.

Kumita, J.R., Poon, S., Caddy, G.L., Hagan, C.L., Dumoulin, M., Yerbury, J.J., Stewart, E.M., Robinson, C.V., Wilson, M.R., and Dobson, C.M. (2007). The extracellular chaperone clusterin potently inhibits human lysozyme amyloid formation by interacting with prefibrillar species. J Mol Biol *369*, 157-167. 10.1016/j.jmb.2007.02.095.

Lai, C., Xie, C., Shim, H., Chandran, J., Howell, B.W., and Cai, H. (2009). Regulation of endosomal motility and degradation by amyotrophic lateral sclerosis 2/alsin. Mol Brain *2*, 23. 10.1186/1756-6606-2-23.

Lapierre, L.R., Silvestrini, M.J., Nunez, L., Ames, K., Wong, S., Le, T.T., Hansen, M., and Melendez, A. (2013). Autophagy genes are required for normal lipid levels in C. elegans. Autophagy *9*, 278-286. 10.4161/auto.22930.

Laplante, M., and Sabatini, David M. (2012). mTOR Signaling in Growth Control and Disease. Cell *149*, 274-293. http://dx.doi.org/10.1016/j.cell.2012.03.017.

Lass, A., Zimmermann, R., Haemmerle, G., Riederer, M., Schoiswohl, G., Schweiger, M., Kienesberger, P., Strauss, J.G., Gorkiewicz, G., and Zechner, R. (2006). Adipose triglyceride lipase-mediated lipolysis of cellular fat stores is activated by CGI-58 and defective in Chanarin-Dorfman Syndrome. Cell Metab *3*, 309-319. 10.1016/j.cmet.2006.03.005.

Layman, A.A.K., Deng, G., O'Leary, C.E., Tadros, S., Thomas, R.M., Dybas, J.M., Moser, E.K., Wells, A.D., Doliba, N.M., and Oliver, P.M. (2017). Ndfip1 restricts mTORC1 signalling and glycolysis in regulatory T cells to prevent autoinflammatory disease. Nat Commun *8*, 15677. 10.1038/ncomms15677.

Lazarou, M., Sliter, D.A., Kane, L.A., Sarraf, S.A., Wang, C.X., Burman, J.L., Sideris, D.P., Fogel, A.I., and Youle, R.J. (2015). The ubiquitin kinase PINK1 recruits autophagy receptors to induce mitophagy. Nature *524*, 309-+. 10.1038/nature14893.

Lee, J.H., Yang, D.S., Goulbourne, C.N., Im, E., Stavrides, P., Pensalfini, A., Chan, H., Bouchet-Marquis, C., Bleiwas, C., Berg, M.J., et al. (2022). Faulty autolysosome acidification in Alzheimer's disease mouse models induces autophagic build-up of A beta in neurons, yielding senile plaques. Nature Neuroscience *25*, 688-+. 10.1038/s41593-022-01084-8.

Lee, J.H., Yu, W.H., Kumar, A., Lee, S., Mohan, P.S., Peterhoff, C.M., Wolfe, D.M., Martinez-Vicente, M., Massey, A.C., Sovak, G., et al. (2010). Lysosomal Proteolysis and Autophagy Require Presenilin 1 and Are Disrupted by Alzheimer-Related PS1 Mutations. Cell *141*, 1146-U1191. 10.1016/j.cell.2010.05.008.

Lee, S., Kim, E., and Park, S.B. (2013). Discovery of autophagy modulators through the construction of a high-content screening platform via monitoring of lipid droplets. Chemical Science *4*, 3282-3287. 10.1039/c3sc51344k.

Lee, S., Sato, Y., and Nixon, R.A. (2011). Primary lysosomal dysfunction causes cargo-specific deficits of axonal transport leading to Alzheimer-like neuritic dystrophy. Autophagy *7*, 1562-1563. 10.4161/auto.7.12.17956.

Li, Y., McGreal, S., Zhao, J., Huang, R.L., Zhou, Y., Zhong, H., Xia, M.H., and Ding, W.X. (2016). A cell-based quantitative high-throughput image screening identified novel autophagy modulators. Pharmacological Research *110*, 35-49. 10.1016/j.phrs.2016.05.004.

Lipinski, M.M., Hoffman, G., Ng, A., Zhou, W., Py, B.F., Hsu, E., Liu, X.X., Eisenberg, J., Liu, J., Blenis, J., et al. (2010). A Genome-Wide siRNA Screen Reveals Multiple mTORC1 Independent Signaling Pathways Regulating Autophagy under Normal Nutritional Conditions. Developmental Cell *18*, 1041-1052. 10.1016/j.devcel.2010.05.005.

Listenberger, L.L., and Brown, D.A. (2007). Fluorescent Detection of Lipid Droplets and Associated Proteins. Current Protocols in Cell Biology *35*, 24.22.21-24.22.11. https://doi.org/10.1002/0471143030.cb2402s35.

Luhr, M., Torgersen, M.L., Szalai, P., Hashim, A., Brech, A., Staerk, J., and Engedal, N. (2019). The kinase PERK and the transcription factor ATF4 play distinct and essential roles in autophagy resulting from tunicamycin-induced ER stress. J Biol Chem *294*, 8197-8217. 10.1074/jbc.RA118.002829.

Ma, X.M., and Blenis, J. (2009). Molecular mechanisms of mTOR-mediated translational control. Nat Rev Mol Cell Biol *10*, 307-318. 10.1038/nrm2672.

Martin, S., and Parton, R.G. (2006). Lipid droplets: a unified view of a dynamic organelle. Nature Reviews Molecular Cell Biology *7*, 373-378. 10.1038/nrm1912.

Martina, J.A., Chen, Y., Gucek, M., and Puertollano, R. (2012). MTORC1 functions as a transcriptional regulator of autophagy by preventing nuclear transport of TFEB. Autophagy *8*, 903-914. 10.4161/auto.19653.

Meléndez, A., Tallóczy, Z., Seaman, M., Eskelinen, E.L., Hall, D.H., and Levine, B. (2003). Autophagy genes are essential for dauer development and life-span extension in C. elegans. Science *301*, 1387-1391. 10.1126/science.1087782.

Metzger, S., Saukko, M., Van Che, H., Tong, L., Puder, Y., Riess, O., and Nguyen, H.P. (2010). Age at onset in Huntington's disease is modified by the autophagy pathway: implication of the V471A polymorphism in Atg7. Hum Genet *128*, 453-459. 10.1007/s00439-010-0873-9.

Murphy, D.J. (2001). The biogenesis and functions of lipid bodies in animals, plants and microorganisms. Progress in Lipid Research *40*, 325-438. 10.1016/s0163-7827(01)00013-3.

Napolitano, G., Esposito, A., Choi, H., Matarese, M., Benedetti, V., Di Malta, C., Monfregola, J., Medina, D.L., Lippincott-Schwartz, J., and Ballabio, A. (2018). mTOR-dependent phosphorylation controls TFEB nuclear export. Nature Communications *9*, 3312. 10.1038/s41467-018-05862-6.

Neumann, S., Chassefeyre, R., Campbell, G.E., and Encalada, S.E. (2017). KymoAnalyzer: a software tool for the quantitative analysis of intracellular transport in neurons. Traffic *18*, 71-88. 10.1111/tra.12456.

Nixon, R.A. (2013). The role of autophagy in neurodegenerative disease. Nature Medicine *19*, 983-997. 10.1038/nm.3232.

Nixon, R.A. (2017). Amyloid precursor protein and endosomal-lysosomal dysfunction in Alzheimer's disease: inseparable partners in a multifactorial disease. Faseb j *31*, 2729-2743. 10.1096/fj.201700359.

Noda, T., and Ohsumi, Y. (1998). Tor, a phosphatidylinositol kinase homologue, controls autophagy in yeast. J Biol Chem *273*, 3963-3966. 10.1074/jbc.273.7.3963.

Novak, I., Kirkin, V., McEwan, D.G., Zhang, J., Wild, P., Rozenknop, A., Rogov, V., Lohr, F., Popovic, D., Occhipinti, A., et al. (2010). Nix is a selective autophagy receptor for mitochondrial clearance. Embo Reports *11*, 45-51. 10.1038/embor.2009.256.

Oakes, J.A., Davies, M.C., and Collins, M.O. (2017). TBK1: a new player in ALS linking autophagy and neuroinflammation. Molecular Brain *10*, 5. 10.1186/s13041-017-0287-x.

Ochaba, J., Lukacsovich, T., Csikos, G., Zheng, S., Margulis, J., Salazar, L., Mao, K., Lau, A.L., Yeung, S.Y., Humbert, S., et al. (2014). Potential function for the Huntingtin protein as a scaffold for selective autophagy. Proceedings of the National Academy of Sciences *111*, 16889-16894. doi:10.1073/pnas.1420103111.

Olzmann, J.A., and Carvalho, P. (2019). Dynamics and functions of lipid droplets. Nat Rev Mol Cell Biol *20*, 137-155. 10.1038/s41580-018-0085-z.

Palmieri, M., Impey, S., Kang, H., di Ronza, A., Pelz, C., Sardiello, M., and Ballabio, A. (2011). Characterization of the CLEAR network reveals an integrated control of cellular clearance pathways. Hum Mol Genet *20*, 3852-3866. 10.1093/hmg/ddr306.

Papassotiropoulos, A., Bagli, M., Kurz, A., Kornhuber, J., Forstl, H., Maier, W., Pauls, J., Lautenschlager, N., and Heun, R. (2000). A genetic variation of cathepsin D is a major risk factor for Alzheimer's disease. Annals of Neurology *47*, 399-403. 10.1002/1531-8249(200003)47:3<399::Aid-ana22>3.0.Co;2-5.

Park, S., Chapuis, N., Bardet, V., Tamburini, J., Gallay, N., Willems, L., Knight, Z.A., Shokat, K.M., Azar, N., Viguié, F., et al. (2008). PI-103, a dual inhibitor of Class IA

phosphatidylinositide 3-kinase and mTOR, has antileukemic activity in AML. Leukemia *22*, 1698-1706. 10.1038/leu.2008.144.

Petcherski, A., Chandrachud, U., Butz, E.S., Klein, M.C., Zhao, W.N., Reis, S.A., Haggarty, S.J., Ruonala, M.O., and Cotman, S.L. (2019). An Autophagy Modifier Screen Identifies Small Molecules Capable of Reducing Autophagosome Accumulation in a Model of CLN3-Mediated Neurodegeneration. Cells *8*. 10.3390/cells8121531.

Pluskal, T., Castillo, S., Villar-Briones, A., and Orešič, M. (2010). MZmine 2: Modular framework for processing, visualizing, and analyzing mass spectrometry-based molecular profile data. BMC Bioinformatics *11*, 395. 10.1186/1471-2105-11-395.

Podlesny-Drabiniok, A., Marcora, E., and Goate, A.M. (2020). Microglial Phagocytosis: A Disease-Associated Process Emerging from Alzheimer's Disease Genetics. Trends in Neurosciences *43*, 965-979. 10.1016/j.tins.2020.10.002.

Pyo, J.O., Yoo, S.M., Ahn, H.H., Nah, J., Hong, S.H., Kam, T.I., Jung, S., and Jung, Y.K. (2013). Overexpression of Atg5 in mice activates autophagy and extends lifespan. Nature Communications *4*, 2300. 10.1038/ncomms3300.

Ramirez, A., Heimbach, A., Gruendemann, J., Stiller, B., Hampshire, D., Cid, L.P., Goebel, I., Mubaidin, A.F., Wriekat, A.L., Roeper, J., et al. (2006). Hereditary parkinsonism with dementia is caused by mutations in ATP13A2, encoding a lysosomal type 5 P-type ATPase. Nature Genetics *38*, 1184-1191. 10.1038/ng1884.

Ravikumar, B., Duden, R., and Rubinsztein, D.C. (2002). Aggregate-prone proteins with polyglutamine and polyalanine expansions are degraded by autophagy. Hum Mol Genet *11*, 1107-1117.

Renna, M., Bento, C.F., Fleming, A., Menzies, F.M., Siddiqi, F.H., Ravikumar, B., Puri, C., Garcia-Arencibia, M., Sadiq, O., Corrochano, S., et al. (2013). IGF-1 receptor antagonism inhibits autophagy. Human Molecular Genetics *22*, 4528-4544. 10.1093/hmg/ddt300.

Renne, M.F., and Hariri, H. (2021). Lipid Droplet-Organelle Contact Sites as Hubs for Fatty Acid Metabolism, Trafficking, and Metabolic Channeling. Front Cell Dev Biol *9*, 726261. 10.3389/fcell.2021.726261.

Roberts, M.A., and Olzmann, J.A. (2020). Protein Quality Control and Lipid Droplet Metabolism. Annu Rev Cell Dev Biol *36*, 115-139. 10.1146/annurev-cellbio-031320-101827.

Roczniak-Ferguson, A., Petit, C.S., Froehlich, F., Qian, S., Ky, J., Angarola, B., Walther, T.C., and Ferguson, S.M. (2012). The transcription factor TFEB links mTORC1 signaling to transcriptional control of lysosome homeostasis. Sci Signal *5*, ra42. 10.1126/scisignal.2002790.

Rubinsztein, D.C., Codogno, P., and Levine, B. (2012). Autophagy modulation as a potential therapeutic target for diverse diseases. Nature Reviews Drug Discovery *11*, 709-U784.

Rubinsztein, D.C., Gestwicki, J.E., Murphy, L.O., and Klionsky, D.J. (2007). Potential therapeutic applications of autophagy. Nature Reviews Drug Discovery *6*, 304-312. 10.1038/nrd2272.

Rubinsztein, D.C., Marino, G., and Kroemer, G. (2011). Autophagy and Aging. Cell *146*, 682-695. 10.1016/j.cell.2011.07.030.

Sardiello, M., Palmieri, M., di Ronza, A., Medina, D.L., Valenza, M., Gennarino, V.A., Di Malta, C., Donaudy, F., Embrione, V., Polishchuk, R.S., et al. (2009). A gene network regulating lysosomal biogenesis and function. Science *325*, 473-477. 10.1126/science.1174447.

Sarkar, S., Davies, J.E., Huang, Z.B., Tunnacliffe, A., and Rubinsztein, D.C. (2007a). Trehalose, a novel mTOR-independent autophagy enhancer, accelerates the clearance of mutant huntingtin and alpha-synuclein. Journal of Biological Chemistry *282*, 5641-5652. 10.1074/jbc.M609532200.

Sarkar, S., Perlstein, E.O., Imarisio, S., Pineau, S., Cordenier, A., Maglathlin, R.L., Webster, J.A., Lewis, T.A., O'Kane, C.J., Schreiber, S.L., and Rubinsztein, D.C. (2007b). Small molecules enhance autophagy and reduce toxicity in Huntington's disease models. Nature Chemical Biology *3*, 331-338. 10.1038/nchembio883.

Sarkar, S., Ravikumar, B., Floto, R.A., and Rubinsztein, D.C. (2009). Rapamycin and mTOR-independent autophagy inducers ameliorate toxicity of polyglutamine-expanded huntingtin and related proteinopathies. Cell Death Differ *16*, 46-56. 10.1038/cdd.2008.110.

Sarraf, S.A., Shah, H.V., Kanfer, G., Pickrell, A.M., Holtzclaw, L.A., Ward, M.E., and Youle, R.J. (2020). Loss of TAX1BP1-Directed Autophagy Results in Protein Aggregate Accumulation in the Brain. Molecular Cell *80*, 779-795.e710. https://doi.org/10.1016/j.molcel.2020.10.041.

Saxton, R.A., and Sabatini, D.M. (2017). mTOR Signaling in Growth, Metabolism, and Disease. Cell *168*, 960-976. 10.1016/j.cell.2017.02.004.

Sengupta, S., Peterson, T.R., and Sabatini, D.M. (2010). Regulation of the mTOR complex 1 pathway by nutrients, growth factors, and stress. Mol Cell *40*, 310-322. 10.1016/j.molcel.2010.09.026.

Seo, J.Y., Lim, S.S., Kim, J., Lee, K.W., and Kim, J.-S. (2017). Alantolactone and Isoalantolactone Prevent Amyloid β25–35-induced Toxicity in Mouse Cortical Neurons and Scopolamine-induced Cognitive Impairment in Mice. Phytotherapy Research *31*, 801-811. https://doi.org/10.1002/ptr.5804.

Settembre, C., Di Malta, C., Polito, V.A., Arencibia, M.G., Vetrini, F., Erdin, S., Erdin, S.U., Huynh, T., Medina, D., Colella, P., et al. (2011). TFEB Links Autophagy to Lysosomal Biogenesis. Science *332*, 1429-1433. 10.1126/science.1204592.

Settembre, C., Fraldi, A., Medina, D.L., and Ballabio, A. (2013). Signals from the lysosome: a control centre for cellular clearance and energy metabolism. Nature Reviews Molecular Cell Biology *14*, 283-296. 10.1038/nrm3565.

Settembre, C., Zoncu, R., Medina, D.L., Vetrini, F., Erdin, S., Erdin, S., Huynh, T., Ferron, M., Karsenty, G., Vellard, M.C., et al. (2012). A lysosome-to-nucleus signalling mechanism senses and regulates the lysosome via mTOR and TFEB. Embo j *31*, 1095-1108. 10.1038/emboj.2012.32.

Sharma, P., Ando, D.M., Daub, A., Kaye, J.A., and Finkbeiner, S. (2012). HIGH-THROUGHPUT SCREENING IN PRIMARY NEURONS. In Imaging and Spectroscopic Analysis of Living Cells: Imaging Live Cells in Health and Disease, P.M. Conn, ed. pp. 331-360. 10.1016/b978-0-12-391856-7.00041-x.

Sidransky, E., Nalls, M.A., Aasly, J.O., Aharon-Peretz, J., Annesi, G., Barbosa, E.R., Bar-Shira, A., Berg, D., Bras, J., Brice, A., et al. (2009). Multicenter analysis of glucocerebrosidase mutations in Parkinson's disease. N Engl J Med *361*, 1651-1661. 10.1056/NEJMoa0901281.

Sidrauski, C., McGeachy, A.M., Ingolia, N.T., and Walter, P. (2015). The small molecule ISRIB reverses the effects of eIF2α phosphorylation on translation and stress granule assembly. eLife *4*, e05033. 10.7554/eLife.05033.

Sikorska, B., Liberski, P.P., Giraud, P., Kopp, N., and Brown, P. (2004). Autophagy is a part of ultrastructural synaptic pathology in Creutzfeldt-Jakob disease: a brain biopsy study. Int J Biochem Cell Biol *36*, 2563-2573. 10.1016/j.biocel.2004.04.014.

Silva, M.C., Cheng, C., Mair, W., Almeida, S., Fong, H., Biswas, M.Helal U., Zhang, Z., Huang, Y., Temple, S., Coppola, G., et al. (2016). Human iPSC-Derived Neuronal Model of Tau-A152T Frontotemporal Dementia Reveals Tau-Mediated Mechanisms of Neuronal Vulnerability. Stem Cell Reports *7*, 325-340. https://doi.org/10.1016/j.stemcr.2016.08.001.

Silva, M.C., Nandi, G.A., Tentarelli, S., Gurrell, I.K., Jamier, T., Lucente, D., Dickerson, B.C., Brown, D.G., Brandon, N.J., and Haggarty, S.J. (2020). Prolonged tau clearance and stress vulnerability rescue by pharmacological activation of autophagy in tauopathy neurons. Nature Communications *11*. 10.1038/s41467-020-16984-1.

Singh, R., Kaushik, S., Wang, Y.J., Xiang, Y.Q., Novak, I., Komatsu, M., Tanaka, K., Cuervo, A.M., and Czaja, M.J. (2009). Autophagy regulates lipid metabolism. Nature *458*, 1131-U1164. 10.1038/nature07976.

Stockwell, S.R., Platt, G., Barrie, S.E., Zoumpoulidou, G., Poele, R.H.T., Aherne, G.W., Wilson, S.C., Sheldrake, P., McDonald, E., Venet, M., et al. (2012). Mechanism-Based Screen for G1/S Checkpoint Activators Identifies a Selective Activator of EIF2AK3/PERK Signalling. Plos One *7*, 16, e28568. 10.1371/journal.pone.0028568.

Stokin, G.B., Lillo, C., Falzone, T.L., Brusch, R.G., Rockenstein, E., Mount, S.L., Raman, R., Davies, P., Masliah, E., Williams, D.S., and Goldstein, L.S.B. (2005). Axonopathy and transport deficits early in the pathogenesis of Alzheimer's disease. Science *307*, 1282-1288. 10.1126/science.1105681.

Thoreen, C.C., Kang, S.A., Chang, J.W., Liu, Q., Zhang, J., Gao, Y., Reichling, L.J., Sim, T., Sabatini, D.M., and Gray, N.S. (2009). An ATP-competitive mammalian target of rapamycin inhibitor reveals rapamycin-resistant functions of mTORC1. J Biol Chem *284*, 8023-8032. 10.1074/jbc.M900301200.

Tian, Y., Chang, J.C., Fan, E.Y., Flajolet, M., and Greengard, P. (2013). Adaptor complex AP2/PICALM, through interaction with LC3, targets Alzheimer's APP-CTF for terminal degradation via autophagy. Proceedings of the National Academy of Sciences of the United States of America *110*, 17071-17076. 10.1073/pnas.1315110110.

Tsukada, M., and Ohsumi, Y. (1993). ISOLATION AND CHARACTERIZATION OF AUTOPHAGY-DEFECTIVE MUTANTS OF SACCHAROMYCES-CEREVISIAE. Febs Letters *333*, 169-174. 10.1016/0014-5793(93)80398-e.

Varalda, M., Antona, A., Bettio, V., Roy, K., Vachamaram, A., Yellenki, V., Massarotti, A., Baldanzi, G., and Capello, D. (2020). Psychotropic Drugs Show Anticancer Activity by Disrupting Mitochondrial and Lysosomal Function. Front Oncol *10*, 562196. 10.3389/fonc.2020.562196.

Vega-Rubin-de-Celis, S., Peña-Llopis, S., Konda, M., and Brugarolas, J. (2017). Multistep regulation of TFEB by MTORC1. Autophagy *13*, 464-472. 10.1080/15548627.2016.1271514.

von Kleist, L., Ariunbat, K., Braren, I., Stauber, T., Storch, S., and Danyukova, T. (2019). A newly generated neuronal cell model of CLN7 disease reveals aberrant lysosome motility and impaired cell survival. Mol. Genet. Metab. *126*, 196-205. 10.1016/j.ymgme.2018.09.009.

Walther, T.C., Chung, J., and Farese, R.V., Jr. (2017). Lipid Droplet Biogenesis. Annu Rev Cell Dev Biol *33*, 491-510. 10.1146/annurev-cellbio-100616-060608.

Wan, H., Wang, Q., Chen, X., Zeng, Q., Shao, Y., Fang, H., Liao, X., Li, H.S., Liu, M.G., Xu, T.L., et al. (2020). WDR45 contributes to neurodegeneration through regulation of ER homeostasis and neuronal death. Autophagy *16*, 531-547. 10.1080/15548627.2019.1630224.

Wang, C., Xiong, M.N.C., Gratuze, M., Bao, X., Shi, Y., Andhey, P.S., Manis, M., Schroeder, C., Yin, Z.R., Madore, C., et al. (2021). Selective removal of astrocytic APOE4 strongly protects against tau-mediated neurodegeneration and decreases synaptic phagocytosis by microglia. Neuron *109*, 1657-+. 10.1016/j.neuron.2021.03.024.

Wang, X., Beugnet, A., Murakami, M., Yamanaka, S., and Proud, C.G. (2005). Distinct signaling events downstream of mTOR cooperate to mediate the effects of amino acids and

insulin on initiation factor 4E-binding proteins. Mol Cell Biol *25*, 2558-2572. 10.1128/mcb.25.7.2558-2572.2005.

Wang, X., Yu, W., Nawaz, A., Guan, F., Sun, S., and Wang, C. (2010). Palmitate induced insulin resistance by PKCtheta-dependent activation of mTOR/S6K pathway in C2C12 myotubes. Exp Clin Endocrinol Diabetes *118*, 657-661. 10.1055/s-0030-1252069.

Watanabe, S., Ilieva, H., Tamada, H., Nomura, H., Komine, O., Endo, F., Jin, S., Mancias, P., Kiyama, H., and Yamanaka, K. (2016). Mitochondria-associated membrane collapse is a common pathomechanism in SIGMAR1- and SOD1-linked ALS. EMBO Molecular Medicine *8*, 1421-1437. https://doi.org/10.15252/emmm.201606403.

Williams, A., Sarkar, S., Cuddon, P., Ttofi, E.K., Saiki, S., Siddiqi, F.H., Jahreiss, L., Fleming, A., Pask, D., Goldsmith, P., et al. (2008). Novel targets for Huntington's disease in an mTOR-independent autophagy pathway. Nature Chemical Biology *4*, 295-305. 10.1038/nchembio.79.

Xia, H.G., Zhang, L., Chen, G., Zhang, T., Liu, J., Jin, M., Ma, X., Ma, D., and Yuan, J. (2010). Control of basal autophagy by calpain1 mediated cleavage of ATG5. Autophagy *6*, 61-66. 10.4161/auto.6.1.10326.

Yang, D.S., Stavrides, P., Saito, M., Kumar, A., Rodriguez-Navarro, J.A., Pawlik, M., Huo, C.F., Walkley, S.U., Saito, M., Cuervo, A.M., and Nixon, R.A. (2014). Defective macroautophagic turnover of brain lipids in the TgCRND8 Alzheimer mouse model: prevention by correcting lysosomal proteolytic deficits. Brain *137*, 3300-3318. 10.1093/brain/awu278.

Yang, Y., Hentati, A., Deng, H.-X., Dabbagh, O., Sasaki, T., Hirano, M., Hung, W.-Y., Ouahchi, K., Yan, J., Azim, A.C., et al. (2001). The gene encoding alsin, a protein with three guanine-nucleotide exchange factor domains, is mutated in a form of recessive amyotrophic lateral sclerosis. Nature Genetics *29*, 160-165. 10.1038/ng1001-160.

Zanusso, G., Polo, A., Farinazzo, A., Nonno, R., Cardone, F., Di Bari, M., Ferrari, S., Principe, S., Gelati, M., Fasoli, E., et al. (2007). Novel prion protein conformation and glycotype in Creutzfeldt-Jakob disease. Arch Neurol *64*, 595-599. 10.1001/archneur.64.4.595.

Zavodszky, E., Seaman, M.N.J., Moreau, K., Jimenez-Sanchez, M., Breusegem, S.Y., Harbour, M.E., and Rubinsztein, D.C. (2014). Mutation in VPS35 associated with Parkinson's disease impairs WASH complex association and inhibits autophagy. Nature Communications *5*, 3828. 10.1038/ncomms4828.

Zhang, L.H., Yu, J., Pan, H.L., Hu, P., Hao, Y., Cai, W.Q., Zhu, H., Yu, A.D., Xie, X., Ma, D.W., and Yuan, J.Y. (2007). Small molecule regulators of autophagy identified by an image-based high-throughput screen. Proceedings of the National Academy of Sciences of the United States of America *104*, 19023-19028. 10.1073/pnas.0709695104.

Zhong, Z.Y., Umemura, A., Sanchez-Lopez, E., Liang, S., Shalapour, S., Wong, J., He, F., Boassa, D., Perkins, G., Ali, S.R., et al. (2016). NF-kappa B Restricts Inflammasome Activation via Elimination of Damaged Mitochondria. Cell *164*, 896-910. 10.1016/j.cell.2015.12.057.

[i] Simon R. Stockwell *et al*, Mechanism-Based Screen for G1/S Checkpoint Activators Identifies a Selective Activator of EIF2AK3/PERK Signalling. *PLoS ONE*, 2012, 7, e28568.

Acknowledgements

This work was substantially supported by 1RF1AG073418-01 to JWK and P01 AG054407 to JWK and Colleagues

Julia Grandjean (RLW lab) for help with RNA-Seq training for LY.